A&A 649, A134 (2021)
https://doi.org/10.1051/0004-6361/202039240

Astronomy & Astrophysics

Core-collapse supernova subtypes in luminous infrared galaxies

E. Kankare[1], A. Efstathiou[2], R. Kotak[1], E. C. Kool[3], T. Kangas[4], D. O'Neill[5], S. Mattila[1], P. Väisänen[6,7], R. Ramphul[6,8], M. Mogotsi[6], S. D. Ryder[9,10], S. Parker[11,12], T. Reynolds[1], M. Fraser[13], A. Pastorello[14], E. Cappellaro[14], P. A. Mazzali[15,16], P. Ochner[17,14], L. Tomasella[14], M. Turatto[14], J. Kotilainen[18,1], H. Kuncarayakti[1,18], M. A. Pérez-Torres[19,20], Z. Randriamanakoto[6], C. Romero-Cañizales[21], M. Berton[18,22], R. Cartier[23], T.-W. Chen[3], L. Galbany[24], M. Gromadzki[25], C. Inserra[26], K. Maguire[27], S. Moran[1], T. E. Müller-Bravo[28], M. Nicholl[29,30], A. Reguitti[13,31,32], and D. R. Young[5]

(Affiliations can be found after the references)

Received 23 August 2020 / Accepted 24 February 2021

ABSTRACT

The fraction of core-collapse supernovae (CCSNe) occurring in the central regions of galaxies is not well constrained at present. This is partly because large-scale transient surveys operate at optical wavelengths, making it challenging to detect transient sources that occur in regions susceptible to high extinction factors. Here we present the discovery and follow-up observations of two CCSNe that occurred in the luminous infrared galaxy (LIRG) NGC 3256. The first, SN 2018ec, was discovered using the ESO HAWK-I/GRAAL adaptive optics seeing enhancer, and was classified as a Type Ic with a host galaxy extinction of $A_V = 2.1^{+0.3}_{-0.1}$ mag. The second, AT 2018cux, was discovered during the course of follow-up observations of SN 2018ec, and is consistent with a subluminous Type IIP classification with an $A_V = 2.1 \pm 0.4$ mag of host extinction. A third CCSN, PSN J10275082−4354034 in NGC 3256, was previously reported in 2014, and we recovered the source in late-time archival *Hubble* Space Telescope imaging. Based on template light curve fitting, we favour a Type IIn classification for it with modest host galaxy extinction of $A_V = 0.3^{+0.4}_{-0.3}$ mag. We also extend our study with follow-up data of the recent Type IIb SN 2019lqo and Type Ib SN 2020fkb that occurred in the LIRG system Arp 299 with host extinctions of $A_V = 2.1^{+0.1}_{-0.3}$ and $A_V = 0.4^{+0.1}_{-0.2}$ mag, respectively. Motivated by the above, we inspected, for the first time, a sample of 29 CCSNe located within a projected distance of 2.5 kpc from the host galaxy nuclei in a sample of 16 LIRGs. We find, if star formation within these galaxies is modelled assuming a global starburst episode and normal IMF, that there is evidence of a correlation between the starburst age and the CCSN subtype. We infer that the two subgroups of 14 H-poor (Type IIb/Ib/Ic/Ibn) and 15 H-rich (Type II/IIn) CCSNe have different underlying progenitor age distributions, with the H-poor progenitors being younger at 3σ significance. However, we note that the currently available sample sizes of CCSNe and host LIRGs are small, and the statistical comparisons between subgroups do not take into account possible systematic or model errors related to the estimated starburst ages.

Key words. galaxies: star formation – supernovae: general – galaxies: individual: NGC 3256 – galaxies: individual: Arp 299 – dust, extinction

1. Introduction

The local (≤12 Mpc) core-collapse supernova (CCSN) population already clearly shows that optical transient survey programmes are not discovering all SNe in normal spiral galaxies due to host galaxy extinction (Mattila et al. 2012), also consistent with statistical studies of galaxy disc opacities (e.g., Kankare et al. 2009). Furthermore, recent surveys operating at longer wavelengths have also discovered SNe missed by optical transient searches in nearby star-forming galaxies, see the SPitzer InfraRed Intensive Transients Survey (SPIRITS; Jencson et al. 2017, 2018, 2019). The effect of a missing population of CCSNe becomes even more prominent in luminous ($10^{11}\,L_\odot < L_{\rm IR} < 10^{12}\,L_\odot$) and ultraluminous ($L_{\rm IR} > 10^{12}\,L_\odot$) infrared galaxies (LIRGs and ULIRGs, respectively) which are highly obscured and star-forming galaxies; it is also very common that these objects are closely paired or merging galaxies (Sanders et al. 1988). Radio observations have shown the existence of a rich population of radio SNe (and SN remnants) in ULIRGs (e.g., Parra et al. 2007; Varenius et al. 2019), LIRGs (e.g., Pérez-Torres et al. 2009; Ulvestad 2009), and starburst galaxies (e.g., Fenech et al. 2008; Mattila et al. 2013), which have remained undetected by optical surveys. In particular, LIRGs are relatively rare in the local Universe; however, they dominate the cosmic star formation history and the resulting CCSN rate beyond $z \sim 1$ (e.g., Magnelli et al. 2011), both of which peak at $z \sim 2$ (Madau & Dickinson 2014).

The Supernovae UNmasked By Infra-Red Detection (SUNBIRD) collaboration (Mattila et al. 2007; Kankare et al. 2008, 2012; Kool et al. 2018; Kool 2019) has carried out systematic survey programmes to discover and study CCSNe in LIRGs using adaptive optics (AO) instruments at the Very Large Telescope (VLT), Gemini, and Keck facilities. The AO observations carried out in high resolution and in the near-IR are an ideal combination to discover obscured CCSNe in crowded and dusty environments of these galaxies. For example, the AO discovery of SN 2008cs, with a derived host galaxy line-of-sight extinction of $A_V \approx 16$ mag, shows that there is a population of very highly reddened CCSNe in these galaxies (Kankare et al. 2008). Furthermore, SNe with very small projected nuclear distances but low host galaxy extinctions can also be missed by regular ground-based observations due to the high background luminosity of the LIRG host (e.g., SN 2010cu; Kankare et al. 2012). Therefore, it is not surprising that optical transient surveys miss a significant fraction of CCSNe in LIRGs even in the local Universe (e.g., Mattila et al. 2012; Kool et al. 2018).

Various statistical studies have been carried out on the properties of CCSNe in normal galaxies. Statistical studies have

shown that Type Ibc SNe are spatially more closely associated with Hα regions than Type IIP SNe, and that within Type Ibc SNe, Type Ic events show the closest Hα association (e.g., Anderson et al. 2012). This has been interpreted as Type Ibc SN progenitors having shorter stellar life times than Type IIP SNe, which is expected from single stellar evolution models. Similar results have also been found by Crowther (2013), Aramyan et al. (2016), and Audcent-Ross et al. (2020), among others. Furthermore, Kangas et al. (2017) corroborated these previous results with their statistical study combining spatial distribution of massive stars to those of different CCSN classes in local galaxies. Other statistical studies on the explosion site have also suggested that Type Ic SNe occur in more metal rich environments and have more massive progenitors than Type Ib SNe (Leloudas et al. 2011; Galbany et al. 2018; Kuncarayakti et al. 2018).

Anderson & Soto (2013) suggested that normal galaxies tend to produce similar SN types if they host multiple SNe, and speculated that this is connected to the episodic nature of the starburst event and the resulting age range distribution of possible SN progenitor stars. LIRGs with their very high SN rates (SNRs) offer laboratories to investigate statistical SN characteristics, with the advantage that the recent and more strongly episodic star formation of the galaxy can be characterised more accurately. Only very recently have CCSN discoveries in central regions of LIRGs made a statistically significant sample (Kool et al. 2018). In the sections that follow we report discoveries of recent CCSNe in LIRGs NGC 3256 and Arp 299, and discuss the starburst age in high CCSN rate LIRGs with a connection to CCSN subtypes in these galaxies.

2. NGC 3256

NGC 3256 is an ongoing LIRG merger at a redshift of $z = 0.009354$ (Wong et al. 2006) with $L_{\rm IR} = 10^{11.61}\,L_{\odot}$ (Sanders et al. 2003) scaled to a Tully–Fisher (TF) luminosity distance of $D_{\rm l} = 37.4$ Mpc (Tully 1988). The adopted TF distance is consistent with the redshift-based distance of 38.6 ± 2.7 Mpc ($H_0 = 70\,{\rm km\,s^{-1}\,Mpc^{-1}}$, $\Omega_{\rm M} = 0.3$, $\Omega_{\Lambda} = 0.7$) corrected for the influence of Virgo Cluster and the Great Attractor infall (Mould et al. 2000). The IR luminosity of NGC 3256 suggests a rate of $\sim$1.1 CCSN yr^{-1} based on the empirical relation of Mattila & Meikle (2001). There is also some evidence of an obscured AGN in the system (Kotilainen et al. 1996; Emonts et al. 2014; Ohyama et al. 2015). While the expected intrinsic SNR of NGC 3256 is very high, only one spectroscopically confirmed SN has been previously reported in this nearby LIRG. This is the Type II SN 2001db, discovered using near-IR observations and found to have a significant line-of-sight extinction of $A_V \approx 5.5$ mag (Maiolino et al. 2002). The Galactic extinction towards the LIRG is $A_V = 0.334$ mag (Schlafly & Finkbeiner 2011).

2.1. SN 2018ec

The High-Acuity Wide field K-band Imager (HAWK-I; Kissler-Patig et al. 2008) on the 8.2 m VLT UT4 consists of four HAWAII 2RG 2048 × 2048 pix near-IR arrays with a total field of view of 7.5′ × 7.5′ and a pixel scale of 0.″106 pix^{-1}. We observed in the Ks-band two LIRGs, NGC 3256 and IRAS 08355−4944, in the European Southern Observatory (ESO) Science Verification (SV) run of HAWK-I with the GRound Layer Adaptive optics Assisted by Lasers module (GRAAL; Paufique et al. 2010). The Tip-Tilt Star-free mode SV observations of NGC 3256 were carried out on 2018 January 3.4 UT (full width at half maximum, $FWHM \sim 0.''4$) and 2018 January 6.4 UT ($FWHM \sim 0.''3$). Previously, it had not been possible to target NGC 3256 with full AO facilities due to the lack of a suitable natural guide star ($m \lesssim 17$ mag) in the field.

The HAWK-I/GRAAL data were reduced in a standard manner for near-IR images, using IRAF[1] based tasks. We discovered a new transient source (SN 2018ec) in NGC 3256 by using an archival ESO New Technology Telescope (NTT) Son of ISAAC (SOFI; Moorwood et al. 1998) Ks-band image from 2003 January 23.2 UT as a reference. We reported the discovery in Kankare et al. (2018a), and spectroscopically classified it as a reddened Type Ic (Berton et al. 2018) via the extended Public ESO Spectroscopic Survey for Transient Objects (ePESSTO; Smartt et al. 2015). The discovery image is shown in Fig. 1. To our knowledge, no optical large-scale sky survey has reported a detection of SN 2018ec; however, this might be due in part to the less monitored southern declination of NGC 3256.

Astrometry of the HAWK-I/GRAAL image was derived using 17 stars selected from the Two Micron All-Sky Survey (2MASS), yielding RA = $10^{\rm h}27^{\rm m}50\overset{\rm s}{.}77$ and Dec = −43°54′06.″3 (equinox J2000.0) for the location of SN 2018ec. This is 5.″2 W and 7.″7 N from the Ks-band nucleus of NGC 3256, and corresponds to a projected distance of 1.7 kpc. Typical for LIRGs, NGC 3256 hosts a large population of super star clusters (see e.g., Trancho et al. 2007), and such structures can very likely contribute to the underlying emission seen at the location of SN 2018ec and other CCSNe in NGC 3256 in the pre-explosion reference images. Spectrophotometric follow-up data of SN 2018ec were obtained with NTT as a part of ePESSTO using the ESO Faint Object Spectrograph and Camera 2 (EFOSC2; Buzzoni et al. 1984) and SOFI. The data were reduced in a standard manner using the PESSTO pipeline (Smartt et al. 2015) based on standard IRAF tasks.

All images were template subtracted using the ISIS2.2 package (Alard & Lupton 1998; Alard 2000). We used H- and Ks-band reference images from FLAMINGOS-2 at Gemini South observed on 2017 March 26.3 and 2017 March 12.1 UT, respectively, while the J-band reference image was taken with SOFI at NTT on 2001 April 9.1 UT. The g, r, i, z-band archival reference images were observed with Dark Energy Camera (DECam; Flaugher et al. 2015) at the 4 m Blanco Telescope on 2017 February 20.3, 2017 February 21.3, 2017 March 18.2, and 2017 February 9.3 UT, respectively. The $JHKs$ images were calibrated using 2MASS magnitudes of stars in the field of SN 2018ec. The gri photometry was calibrated using the American Association of Variable Star Observers (AAVSO) Photometric All-Sky Survey magnitudes for stars in the large field of DECam images which were then used to yield magnitudes for 15 sequence stars close to SN 2018ec; these stars are shown in Fig. A.1 and the magnitudes are listed in Table A.1. The z-band sequence stars were calibrated using standard star field observations carried out with NTT. The point spread function (PSF) photometry of the SN was carried out using the QUBA pipeline (Valenti et al. 2011). The photometry is listed in Table A.2 with the $griz$ magnitudes in the AB system and JHK magnitudes in the Vega system.

Ryder et al. (2018) reported radio observations of the field of SN 2018ec with the Australia Telescope Compact Array (ATCA) on 2018 January 23.8 UT. The observations yielded 3σ upper limits at the location of SN 2018ec of <10 mJy beam^{-1} and

[1] IRAF is distributed by the National Optical Astronomy Observatories, which are operated by the Association of Universities for Research in Astronomy, Inc., under cooperative agreement with the National Science Foundation.

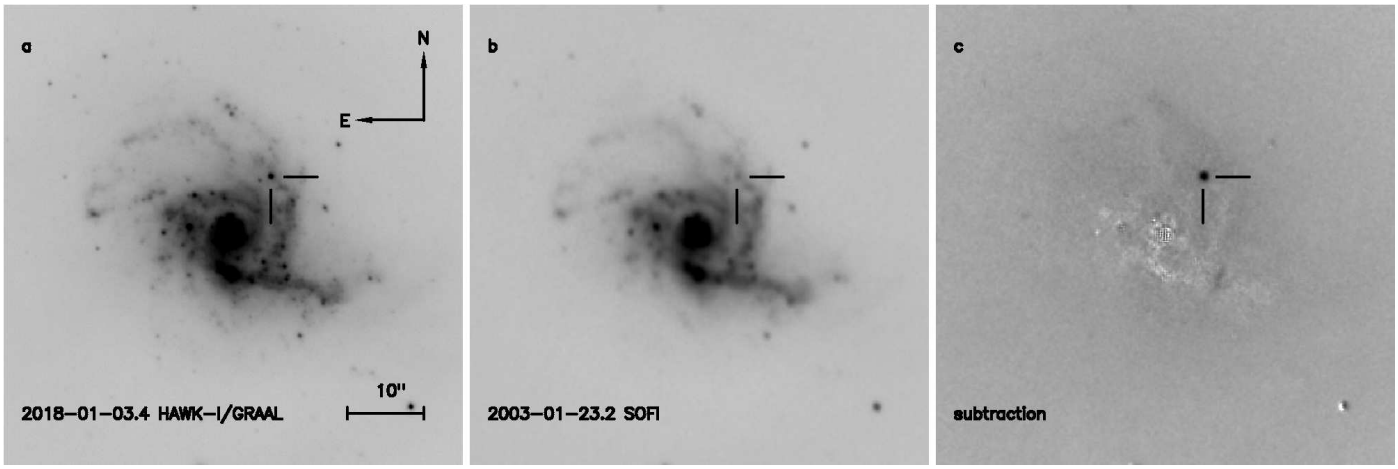

Fig. 1. Subsection images ($1' \times 1'$) of the field of SN 2018ec in NGC 3256. *a*) HAWK-I/GRAAL *Ks*-band discovery image of SN 2018ec, *b*) SOFI reference image, and *c*) Subtraction between the images. The AO enhanced HAWK-I/GRAAL image with $FWHM \sim 0\farcs4$ has a superior image quality compared to the normal ground-based seeing SOFI image with $FWHM \sim 0\farcs8$. The location of SN 2018ec is shown with tick marks in all the panels; the orientation and image scale are indicated in the *first panel*.

<3.6 mJy beam^{-1} at 5.5 and 9.0 GHz, respectively. This corresponds to $<6.0 \times 10^{27}$ erg s^{-1} Hz^{-1} at 9 GHz; the limit is above the peak of normal Type Ic SNe around 10^{26}–10^{27} erg s^{-1} Hz^{-1} (e.g., Romero-Cañizales et al. 2014, and references therein). The limits are not particularly constraining, due to the high background radio emission of the host galaxy. Further radio limits were reported by Nayana & Chandra (2018) based on observations with the Giant Metrewave Radio Telescope (GMRT) at 1.39 GHz on 2018 January 20.9 UT, yielding a 3σ upper limit of 2.1 mJy ($<3.5 \times 10^{27}$ erg s^{-1} Hz^{-1}) at the SN 2018ec location.

SN 2018ec is found to be spectroscopically a normal Type Ic SN, and in our analysis we find a similarity to SN 2007gr (Hunter et al. 2009), see below. The line-of-sight host galaxy extinction of SN 2018ec was estimated using a χ^2 fit of broad-band light curves of SN 2018ec with those of SN 2007gr (including an extrapolation of the optical late-time light curves of SN 2007gr based on the data beyond +70 d using linear fits). The fit was carried out simultaneously in all the bands with follow-up data of SN 2018ec. The method is the same as that used in Kankare et al. (2014a), among others. The free parameters of the fit are the host galaxy line-of-sight extinction A_V, the discovery epoch t_0 relative to a suitable reference (the estimated explosion date or light curve maximum), and fixed constant shift C applied to all the bands representing the intrinsic differences in the brightness of SNe (and any systematic difference in the distance estimates of the two SNe). The Johnson-Cousins *UBVRI* light curves of SN 2007gr (Hunter et al. 2009) were converted into the *griz* system with the transformations of Jester et al. (2005). We adopted the well-established Cardelli et al. (1989) extinction law for the fitting. The errors of the data points in the analysed light curves are considered Gaussian. If the light curves are well sampled and the comparison SN is well suited for the comparison, the probability density functions of the fitted parameters follow approximately Gaussian distributions. The largest deviations from this typically occur within the error of t_0 if the light curve follow-up was initiated post-maximum. The reported errors correspond to 68.3 % confidence intervals estimated based on the probability density functions; systematic errors related to the uncertainty of the host extinction of the comparison SN are not included in the reported values. Based on the comparison with SN 2007gr we conclude that SN 2018ec was discovered 19^{+13}_{-3} days after optical maximum, has a host galaxy extinction of $A_V = 2.1^{+0.3}_{-0.1}$ mag, and is $C = 0.6^{+0.4}_{-0.2}$ mag brighter than SN 2007gr. The absolute magnitude light curves are shown in Fig. 2. Based on the fit we estimate that SN 2018ec peaked at $M_r \approx -18$ mag; this is at the brighter end of the peak magnitude distribution of normal Type Ic SNe but not unusual (e.g., Taddia et al. 2018).

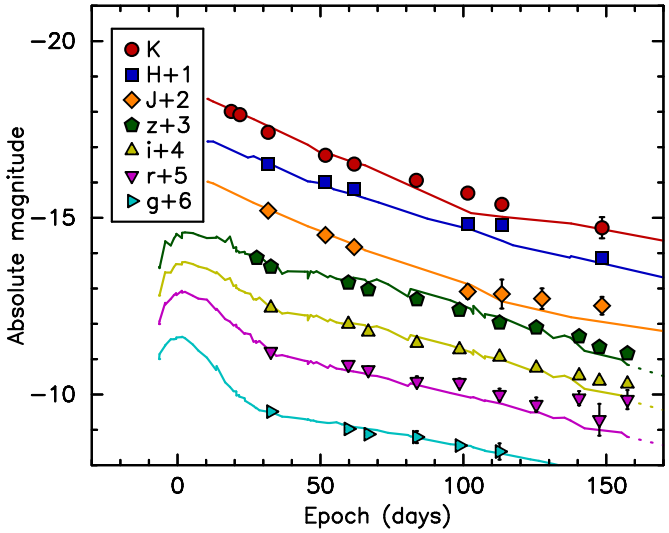

Fig. 2. Absolute magnitude light curves of SN 2018ec after correcting for host extinction ($A_V = 2.1$ mag). The light curves of the Type Ic SN 2007gr are shown with solid lines, and are shifted vertically by −0.58 mag (optical light curves extrapolated with linear fits for comparison are indicated with dotted curves). The estimated errors for most light curve points are smaller than the symbol size. The epoch 0 is the *B*-band maximum estimated for SN 2007gr by Hunter et al. (2009).

The spectroscopic sequence of SN 2018ec is shown in Fig. 3, also illustrating the similarity to the normal Type Ic SN 2007gr (Hunter et al. 2009). Following a more detailed classification scheme by Prentice & Mazzali (2017), SN 2018ec appears to be a Ic-6/7. The most prominent SN feature is the Ca II near-IR triplet. The typically strong O I λ7772 line in Type Ib/c SNe is blended with the telluric *A*-band feature. No clear He I features arising from the SN are evident, supporting a Type Ic classification. Actually there are broad P Cygni

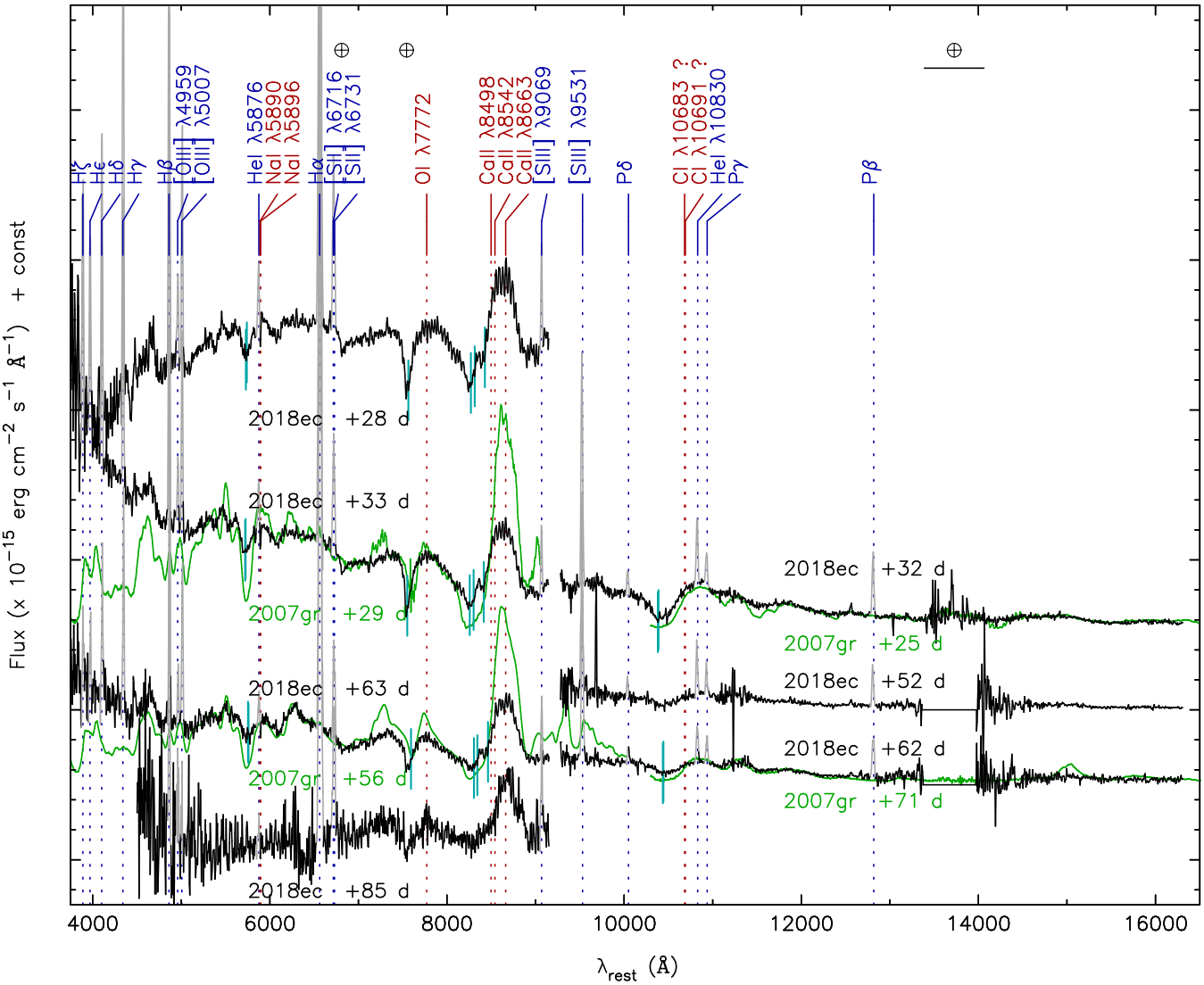

Fig. 3. Spectral time series of SN 2018ec. The spectra have been redshift corrected to rest frame. The spectra have been corrected for both Galactic $A_V = 0.334$ mag and estimated host galaxy extinction of $A_V = 2.1$ mag. The epochs are provided respective to the estimated light curve maximum. The main narrow-line emission features arising from an incomplete host galaxy subtraction are in grey. The most prominent identified spectral features are labelled coming either from the SN (red) or from the host galaxy (blue). The Doppler shifted position of the SN lines are indicated with cyan vertical lines in selected epochs as suggested by the velocity of the Na I absorption minimum. The main telluric bands are indicated with a circled plus sign (⊕). For comparison selected spectra of normal Type Ic SN 2007gr are overlaid (green). The continua of the optical spectra of SN 2018ec are likely contaminated by the complex host background that was not successfully completely subtracted. Therefore, the optical SN features of SN 2018ec above and below the continuum level appear less prominent than those of SN 2007gr. The spectra have been shifted vertically for clarity.

profiles close to the rest wavelengths of He I λ5876 and λ10830 lines, but these features can also be associated with Na I D and C I $\lambda\lambda$10683,10691, respectively. These lines have an absorption minimum at ∼8500 km s^{-1} around +33 d, which declines to ∼7000 km s^{-1} within ∼1 month, see Fig. 4. As minor differences compared to SN 2007gr, SN 2018ec does not show early C I $\lambda\lambda$11330,11753 features, or Si II λ6355 absorption feature around +32 d. Furthermore, the Mg I λ15687 emission feature is not visible in the +62 d spectrum of SN 2018ec.

2.2. AT 2018cux

During the ePESSTO follow-up of SN 2018ec the EFOSC2 data led to a serendipitous discovery of another transient AT 2018cux in NGC 3256 using images obtained on 2018 March 24.2 UT in comparison to images from 2018 January 17.2 UT as a reference. The discovery was reported in Kankare et al. (2018b) and the *i*-band discovery image is shown in Fig. 5. We find coordinates RA = 10^{h}27^{m}51^s.41 and Dec = −43°54′18″.0 (equinox J2000.0) for AT 2018cux from the EFOSC2 images processed by the PESSTO pipeline. This corresponds to 1″.7 E and 4″.0 S of the host galaxy main *Ks*-band nucleus. This translates to a projected distance of 0.8 kpc. The location of AT 2018cux is relatively close to, but not coincident with the southern nucleus of NGC 3256, located at RA = 10^{h}27^{m}51^s.22 and Dec = −43°54′19″.2 (equinox J2000.0) based on radio observations (Neff et al. 2003). However, this southern nucleus is heavily obscured at optical and near-IR wavelengths by dust and thus the association of AT 2018cux observed in optical wavelengths to this component is uncertain. The PSF photometry of AT 2018cux was carried

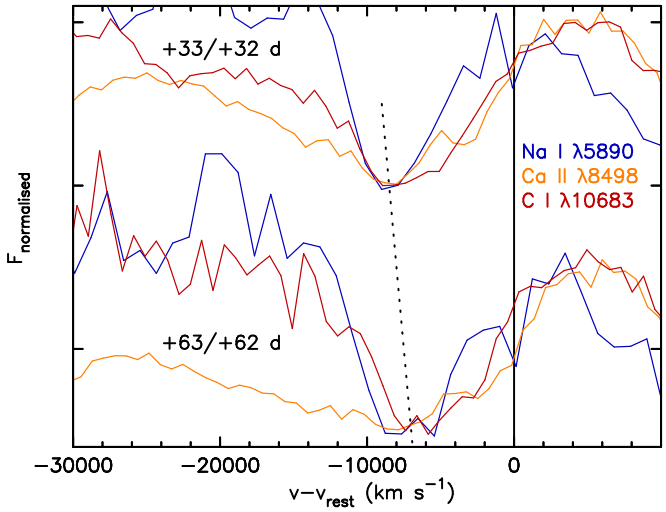

Fig. 4. Prominent P Cygni features of SN 2018ec at two selected epochs. The zero velocity is set to the rest wavelength of the shortest wavelength component of each line blend, i.e., at 5890 Å for the Na I D (blue), 8498 Å for the Ca II near-IR triplet (orange), and 10683 Å for a C I blend (red). Velocities at absorption minima shown by the features are surprisingly similar, with ∼8500 km s^{-1} around ∼1 month from the estimated maximum light and ∼7000 km s^{-1} at ∼2 months from light curve peak, with the latter epoch showing somewhat more scatter, which can (partly) arise from the lower signal-to-noise ratio of the spectra. The spectra are binned by a factor of 4, for clarity and the line profiles are normalised to match the flux level of both their absorption minimum and emission peak within a given epoch.

out similar to that of SN 2018ec and is listed in Table A.4. Late-time long-slit spectroscopy of AT 2018cux was obtained on 2018 July 3.7 UT with the Southern African Large Telescope (SALT; Buckley et al. 2006) using the Robert Stobie Spectrograph (RSS; Burgh et al. 2003; Kobulnicky et al. 2003). The spectrum was reduced in a standard manner with basic IRAF tasks.

We used an approach similar to that previously described for SN 2018ec to estimate the host galaxy extinction for AT 2018cux. The transient shows flat and plateau-like light curves, with colours that are only somewhat reddened in combination with relatively faint magnitudes, which suggest a subluminous Type IIP SN (e.g., Spiro et al. 2014; Müller-Bravo et al. 2020). This is also supported by our one low signal-to-noise ratio spectrum of the event (see next paragraph). Therefore, SN 2005cs (Pastorello et al. 2009) was adopted as a canonical reference example of a normal subluminous Type IIP SN, with the optical light curves transferred into the *griz* system with the Jester et al. (2005) conversions. Based on the comparison fit, AT 2018cux was found to be most consistent with a host galaxy extinction of $A_V = 2.1 \pm 0.4$ mag, a discovery 6^{+7}_{-3} d after the explosion, and a $0.6^{+0.4}_{-0.3}$ mag fainter plateau (see Fig. 6). With the estimated line-of-sight extinction, at around +50 d from the explosion, the plateau magnitudes reach $M \approx -14.5$ mag in *riz* bands. However, the faintest subluminous Type IIP events like SNe 1999br and 2001dc have plateau magnitudes of $M_V \approx -13.6$ and -14.3 mag, respectively (Pastorello et al. 2004). Similarly, the absolute magnitudes of AT 2018cux are generally brighter than those of faint transients that are interpreted as SN impostors (i.e., non-terminal outbursts of massive stars) (see e.g., Smith et al. 2011). AT 2018cux is also brighter compared to transients such as SN 2008S that have been associated either with a SN impostor or an electron-capture SN origin (Prieto et al. 2008; Botticella et al. 2009; Smith et al. 2009).

Based on the estimated explosion epoch of AT 2018cux, the SALT spectrum of the site of AT 2018cux was obtained at $+108^{+7}_{-3}$ d. In Fig. 7 the SALT spectrum is shown corrected for extinction, overlaid with an arbitrarily shifted +106 d spectrum of SN 2005cs at the end of the plateau phase, consistent with a subluminous Type IIP SN classification. In particular, typical features for subluminous Type IIP SNe are the flux attenuation below ∼5500 Å, and the absorption feature around 6150–6300 Å consistent with a blend of Sc II and Ba II lines.

2.3. PSN J10275082−4354034

In addition to SN 2001db, SN 2018ec, and AT 2018cux in NGC 3256, an SN candidate PSN J10275082−4354034 (hereafter PSN102750) was reported[2] in 2014 in the same LIRG at RA = $10^h27^m50^s.82$ and Dec = −43°54′03″.4, discovered by Peter Aldous at Geraldine Observatory[3]. Based on the coordinates, the projected distance of the transient from the *Ks*-band nucleus is 2.1 kpc. An unfiltered discovery magnitude on 2014 May 7.45 UT of 15.6 mag was reported. Unfortunately, no spectroscopic classification of the transient was carried out by anyone to our knowledge.

Follow-up imaging of PSN102750 was carried out by S. Parker. This included one epoch of luminance filter observations using the 50 cm T30 telescope[4] with FLI-PL6303E CCD camera at the Siding Springs Observatory, and two epochs of unfiltered observations with a 35 cm Celestron C14 reflector and SBIG ST-10 CCD camera at the Parkdale Observatory. The data reduction included basic bias and dark subtraction steps and flat fielding. The QUBA pipeline was used to carry out the PSF photometry of the SN candidate by calibrating the images directly into *R* band (see Table A.5).

Furthermore, we recovered PSN102750 in *Hubble* Space Telescope (HST) archival images obtained with the Wide Field Camera 3 (WFC3). NGC 3256 was observed in the *F467M* (Strömgren *b*) and *F621M* filters on 2014 June 10 and 2014 November 13, respectively[5]. Figure 8 clearly shows the late-time detection of PSN102750 in comparison to an archival image obtained with a similar filter. Photometry on the images with the transient was carried out using DOLPHOT[6], an HST dedicated photometry package. The individual charge transfer efficiency (CTE) corrected images were masked for bad pixels and the sky background was fitted and subtracted, before being aligned to produce the drizzle-combined image. PSFs were then fit to all the identified sources present in the images, yielding their magnitude values. The magnitudes of the SN candidate in *F467M* and *F621M* filters were adopted as those of *B* and *R*, respectively.

The resulting light curve of PSN102750 was template fitted with the same method that was used for SN 2018ec and AT 2018cux; however, a selection of different CCSN subtypes was used as templates to yield a tentative classification and host galaxy extinction for the transient. The comparison events include Type IIn SNe 1998S (Fassia et al. 2000; Liu et al. 2000) and 2005ip (Stritzinger et al. 2012), a normal Type IIP SN 2004et (Sahu et al. 2006), and a normal Type Ic SN 2007gr

[2] Reported at the Central Bureau for Astronomical Telegrams Transient Objects Confirmation Page: http://www.cbat.eps.harvard.edu/unconf/followups/J10275082-4354034.html
[3] https://geraldineobservatory.co.nz/
[4] https://support.itelescope.net/support/solutions/articles/231917-telescope-30
[5] Programme 13333, PI: Rich.
[6] http://americano.dolphinsim.com/dolphot/

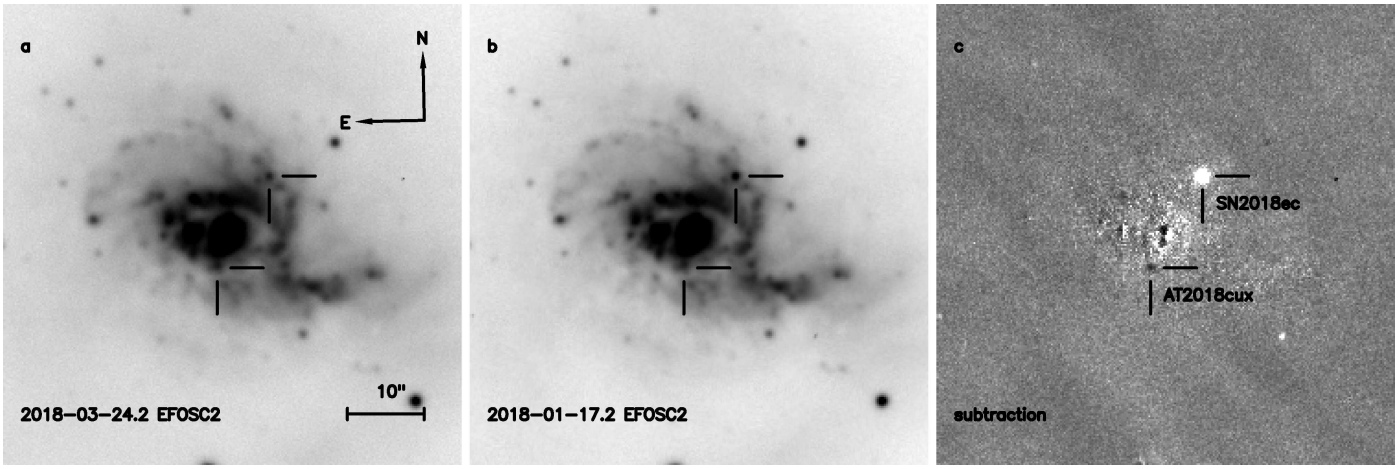

Fig. 5. Subsection images ($1' \times 1'$) of the field of AT 2018cux in NGC 3256. *a*) EFOSC2 *i*-band discovery image ($FWHM \sim 0''.9$) of AT 2018cux, *b*) EFOSC2 pre-discovery image ($FWHM \sim 0''.8$), and *c*) Subtraction between the images. The locations of SN 2018ec and AT 2018cux are shown with tick marks in all the panels. Since the reference image contains increased flux from SN 2018ec compared to that of the AT 2018cux discovery image, the colour scale of the two events is reversed in the subtraction. The image scale and orientation are indicated in the *left panel*.

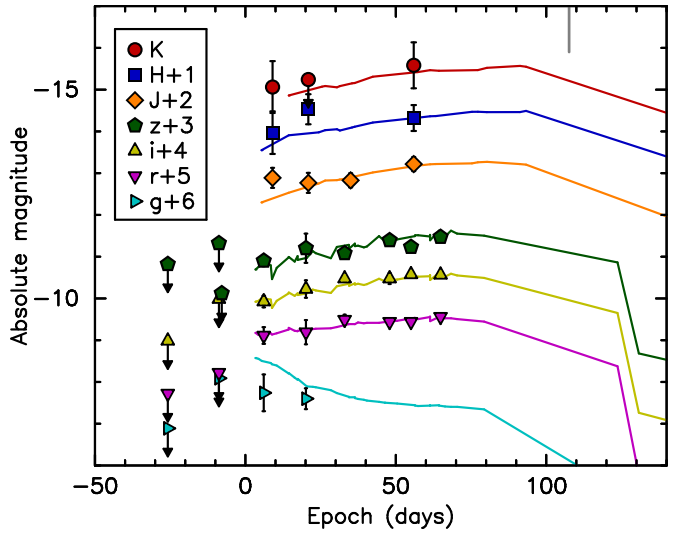

Fig. 6. Absolute magnitude light curves of AT 2018cux including an estimated host galaxy extinction of $A_V = 2.1$ mag. The light curves of the subluminous Type IIP SN 2005cs (Pastorello et al. 2009) are shown with solid lines and shifted vertically by +0.57 mag. The grey vertical line indicates the epoch of the SALT spectrum. The epoch 0 is set to the estimated explosion date of SN 2005cs.

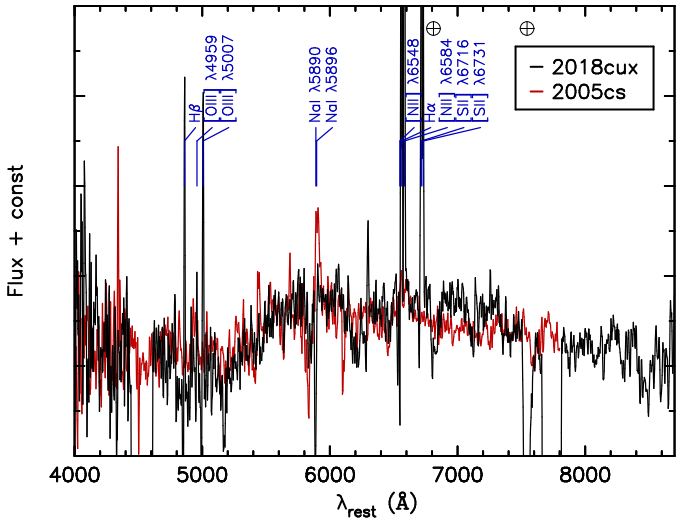

Fig. 7. SALT spectrum (black) at the location of AT 2018cux corrected for host galaxy extinction of $A_V = 2.1$ mag. The overlaid (red) +106 d spectrum of the subluminous Type IIP SN 2005cs (Pastorello et al. 2009) is shifted with an arbitrary added constant and shows overall similarity to that of the AT 2018cux observations. The spectra have been redshift corrected to rest frame. The most prominent host lines of NGC 3256 are indicated. The main telluric bands are indicated with a circled plus sign (⊕).

(Hunter et al. 2009). Furthermore, a comparison to the normal Type Ia SN 2011fe (Munari et al. 2013) was also carried out. The fits are shown in Fig. 9. Comparisons suggest that PSN102750 is most consistent with a Type IIn event (which generally show major diversity in their late-time evolution). Our best fit is with SN 1998S, with PSN102750 discovered shortly before the peak magnitude. However, a Type IIP SN cannot be fully excluded either, though the early photometry of PSN102750 shows deviations from a flat plateau. H-poor stripped-envelope events are excluded based on the blue colours of PSN102750 even if a negligible host extinction is assumed; increasing the extinction would only make the discrepancy larger. A Type Ia SN classification can be excluded primarily based on the bright late-time detection of PSN102750. Based on the light curve fit with SN 1998S as a template, we conclude that PSN102750 has a host galaxy extinction of $A_V = 0.3^{+0.4}_{-0.3}$ mag, is $1.6^{+0.1}_{-0.4}$ mag fainter than SN 1998S, and discovered at -9^{+2}_{-3} days relative to the light curve peak of SN 1998S assuming the extinction law of Cardelli et al. (1989). For comparison, the Type IIP fit using SN 2004et as a template yields $A_V = 0.0^{+0.3}_{-0.0}$ mag, a very small brightness difference of $0.1^{+0.3}_{-0.1}$ mag, and $t_0 = 12^{+2}_{-4}$ days relative to the estimated explosion date. SN 2004et is at the bright end of the intrinsic magnitude distribution of normal Type IIP SNe at plateau (Anderson et al. 2014).

3. Arp 299

Arp 299 is a nearby LIRG at a distance of 44.8 Mpc (Huo et al. 2004). The IR luminosity of the galaxy, $L_{\rm IR} = 10^{11.82}\,L_\odot$ (Sanders et al. 2003), suggests a rate of ~1.8 CCSN yr^{-1} based

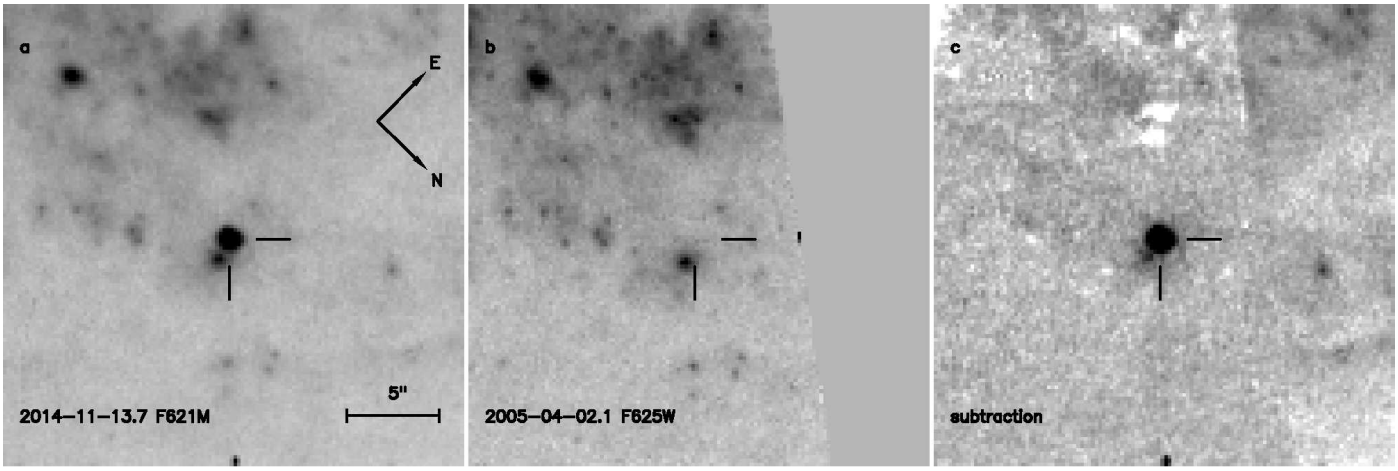

Fig. 8. Subsection images of the field of PSN102750. *a*) Late-time HST *F621M* image of PSN102750 observed 190 d after the discovery of the transient, *b*) Pre-explosion HST *F625W* image of the field of the transient, and *c*) Subtraction between the images. In addition to the event, the subtraction also results in some faint residuals from sources in the field, likely due to the somewhat different filter widths of the two epochs of observations. The transient locations are shown with tick marks. The orientation and image scale are indicated in the *left panel*.

on the empirical relation of Mattila & Meikle (2001). The Galactic extinction towards Arp 299 is $A_V = 0.046$ mag (Schlafly & Finkbeiner 2011). The recent SNe 2019lqo and 2020fkb presented here increase the total number of spectroscopically classified CCSNe in Arp 299 to eight events, in addition to one unclassified near-IR discovered SN 1992bu (see e.g., Mattila et al. 2012).

3.1. SN 2019lqo

SN 2019lqo was discovered on 2019 July 21 07:33:36 UT (JD = 2458685.81500) by the photometric instrument on board the *Gaia* spacecraft, and reported on behalf of the science alerts team as Gaia19dcu (Hodgkin et al. 2019). The *Gaia* *G*-band AB discovery magnitude of SN 2019lqo was 18.33 ± 0.20 mag, with a reported non-detection of $m_G > 21.5$ mag on 2019 July 16 05:26:52 UT (JD = 2458680.72699). The coordinates of the transient provided by *Gaia* are RA = $11^h28^m32\overset{s}{.}460$ and Dec = +58°33′44″.82 (equinox J2000.0), pointing to component A as the likely host (Fig. 10) of Arp 299. This yields a projected distance of 9″.3 from the nucleus of Arp 299-A (Romero-Cañizales et al. 2011) for SN 2019lqo, corresponding to 2.0 kpc. We classified SN 2019lqo within the Nordic Optical Telescope (NOT) Unbiased Transient Survey 2 (NUTS2) on 2019 July 24.9 UT as a young Type IIb SN (Bose et al. 2019). Spectroscopic observations lasting 1800 s were obtained with the Andalucia Faint Object Spectrograph and Camera (ALFOSC) using the low-resolution grism 4 and 1″.0 slit. Another epoch of spectroscopy was obtained with the same setup on 2019 August 2.9 UT.

SN 2019lqo was discovered shortly before the field moved into conjunction with the Sun. However, we were able to obtain multi-band light curve follow-up of the event around the light curve maximum, and observed some additional data points in the tail phase of the SN when the field became observable again. All the optical ALFOSC data were reduced in a standard manner using the QUBA pipeline. The NOT near-IR Camera and spectrograph (NOTCam) imaging was reduced by making use of the external NOTCAM package[7] for IRAF. The QUBA pipeline PSF photometry of SN 2019lqo was calibrated with the sequence star magnitudes obtained from Kankare et al. (2014b). The resulting photometry is listed in Table A.6.

The first Zwicky Transient Facility (ZTF; Bellm et al. 2019) detections of SN 2019lqo (with an internal name ZTF19abgbbzy) are reported on the Transient Name Server; additional ZTF limits and detections are also available, for example via the public MARS broker[8]. Intriguingly, the first reported ZTF detection of $m_r = 18.86$ mag was obtained 24.7 h before the reported *Gaia* non-detection of >21.5 mag. While a SN light curve can evolve extremely rapidly during a very short shock breakout phase, the most likely case here is that a combination of a crowded LIRG background, a faint SN, and a non-optimal *Gaia* sky scanning angle made the SN non-detectable, and resulted in the reported non-detection with a nominal limit. Furthermore, ZTF reports an *r*-band non-detection of >19.5 mag following their initial detection, and two days before the *Gaia* discovery epoch. However, the magnitude limits reported by ZTF are difference image estimates over the whole CCD quadrant (Masci et al. 2019). The location of SN 2019lqo is quite crowded; the luminous galaxy background makes image subtraction challenging and dependent on sky conditions. Therefore, it is not surprising that a limit yielded globally for the field is overly optimistic for the location of SN 2019lqo if the subtraction is not optimal. We proceeded to download the science data product files (Masci et al. 2019) from the ZTF data release 3 (DR3)[9] covering the follow-up of SN 2019lqo and corresponding template reference images. We carried out image subtractions using the ISIS2.2 package, and the resulting PSF photometry for SN 2019lqo, calibrated against the Sloan Digital Sky Survey (SDSS), is listed in Table A.7 for epochs for which we found a >3σ detection. This includes our measurements of $m_r = 19.04 \pm 0.09$ mag for the first ZTF epoch and 18.77 ± 0.12 mag for the epoch following the first detection for which a non-detection was previously reported.

Similar to the SNe in NGC 3256, the line-of-sight extinction of SN 2019lqo was estimated with a simultaneous χ^2 comparison of *UBVRIJHK* light curves to those of well-sampled

[7] http://www.not.iac.es/instruments/notcam/guide/observe.html

[8] https://mars.lco.global/109717499/

[9] https://www.ztf.caltech.edu/page/dr3

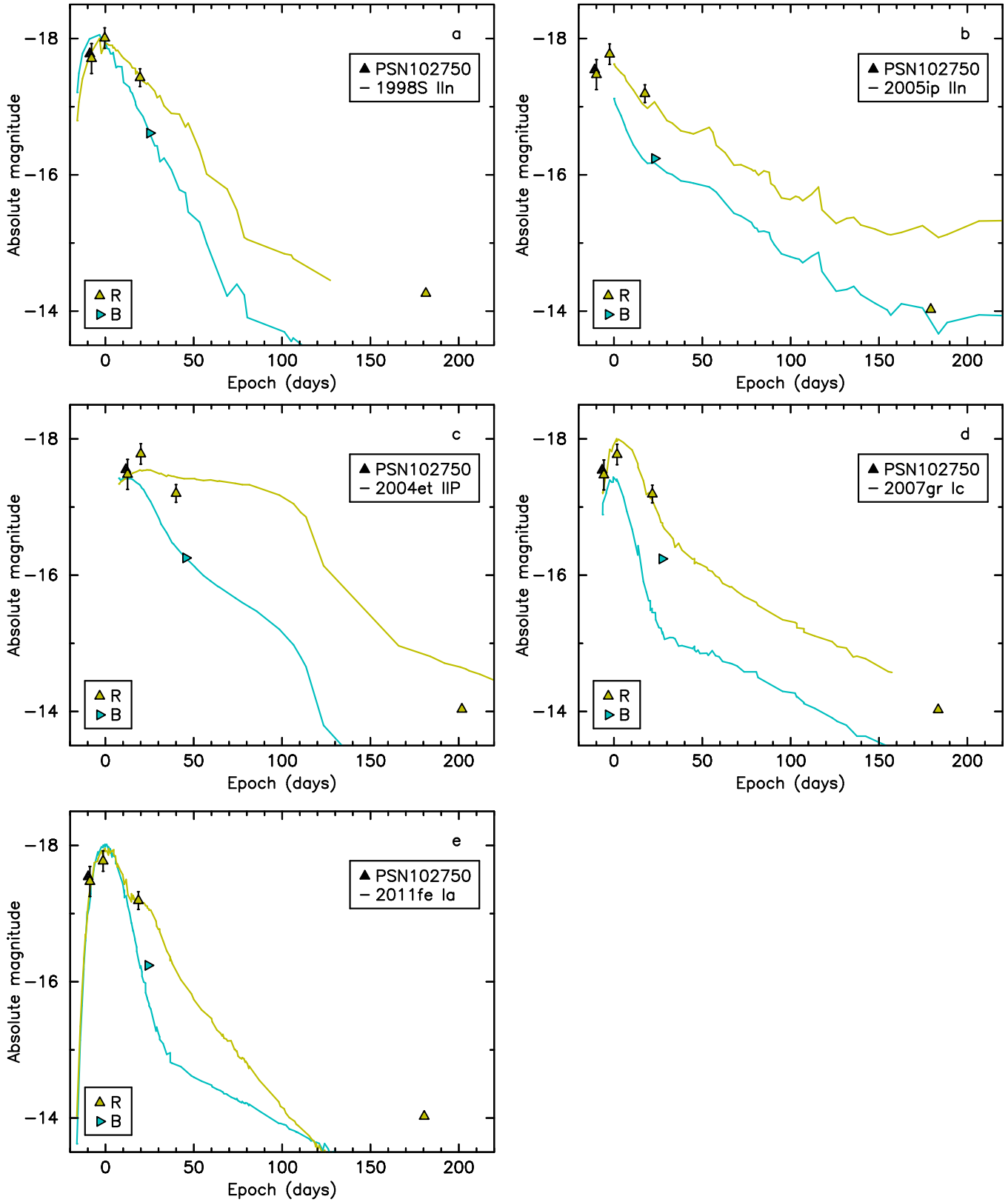

Fig. 9. PSN102750 light curve comparisons to those of *a*) Type IIn SN 1998S, *b*) Type IIn SN 2005ip, *c*) Type IIP SN 2004et, *d*) Type Ic SN 2007gr, and *e*) Type Ia SN 2011fe. The reported unfiltered discovery magnitude is also shown in the plot as a black symbol.

Type IIb SNe 2011dh (Arcavi et al. 2011; Ergon et al. 2014, 2015) and 1993J (Pressberger et al. 1993; Ripero et al. 1993; Richmond et al. 1994, 1996). The fitting was carried out with the Cardelli et al. (1989) extinction law. The resulting absolute magnitude light curves are shown in Fig. 11, including photometry based on publicly available data. The early public

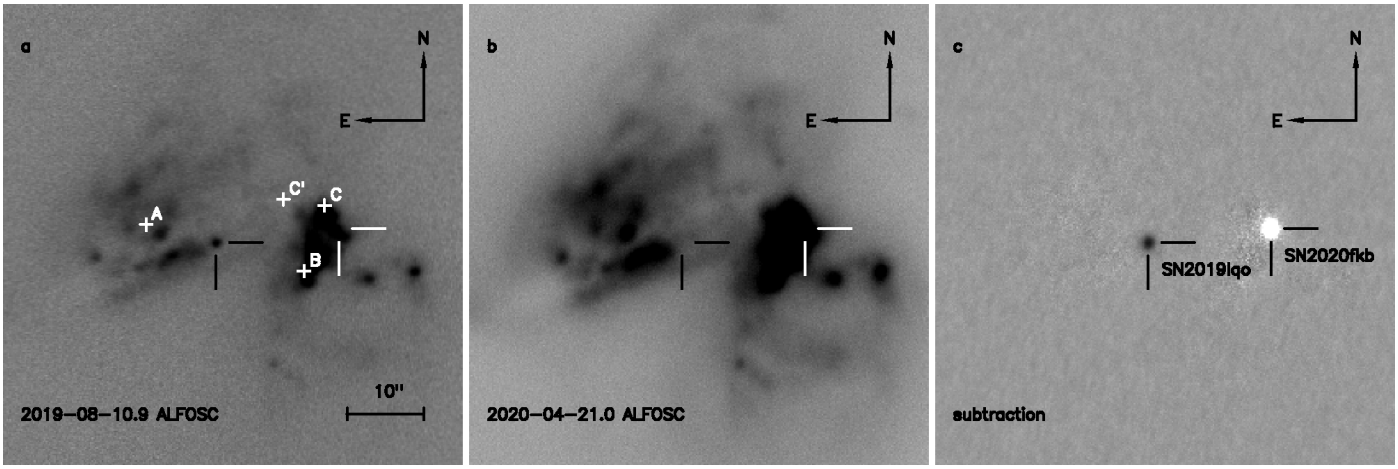

Fig. 10. Subsection images (1′ × 1′) of the field of Arp 299. *a*) NOT *V*-band follow-up image of SN 2019lqo, *b*) NOT follow-up image of SN 2020fkb, and *c*) Subtraction between the images. The tick marks indicate the locations of SNe 2019lqo and 2020fkb. The image scale and orientation are indicated in the *left panel*. The locations of IR bright main components (A, B, C, C′) of Arp 299 (Gehrz et al. 1983) illustrate that some of these regions are obscured in optical wavelengths.

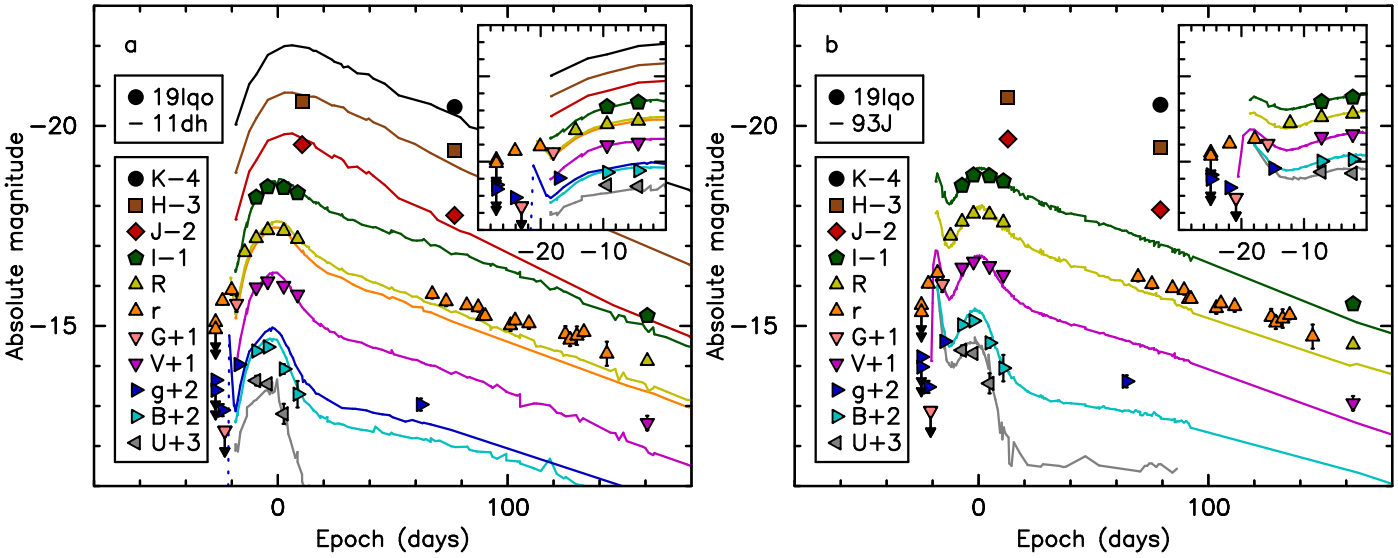

Fig. 11. SN 2019lqo light curve fits to Type IIb SNe *a*) 2011dh and *b*) 1993J. The insets zoom in on the pre-maximum light curves that suggest a relatively long shock cooling phase. The epoch 0 is set to the estimated *R*-band peak.

gGr-band detections of SN 2019lqo suggest that the SN had a relatively long rise time and was discovered possibly during a post-shock cooling phase, more similar to that of SN 1993J than the more rapidly evolving SN 2011dh, but this is poorly constrained. The fit with SN 1993J as a template is superior compared to that of SN 2011dh as a reference; this fit suggests that SN 2019lqo has a host galaxy extinction of $A_V = 2.1^{+0.1}_{-0.3}$ mag, is $0.2^{+0.1}_{-0.3}$ mag brighter than SN 1993J, and peaked in *R* band around JD = 2458702 ± 1 (i.e., around 2019 August 6). There is uncertainty on the host galaxy extinction of SN 1993J and an average value of $E(B-V) = 0.2$ mag was adopted here for the comparison. The rise of the SN 2019lqo light curve appears to be relatively long compared to those of SNe 1993J and 2011dh, and also the post-maximum decline is slightly slower in comparison to these prototypical Type IIb SNe. Intriguingly, SN 2019lqo is spectroscopically more similar to SN 2011dh; for example, it has more prominent absorption features of H I and Ca II near-IR triplet lines compared to SN 1993J (Fig. 12). Therefore, it seems that SN 2019lqo bridges the observational characteristics of these two canonical Type IIb SNe.

3.2. SN 2020fkb

SN 2020fkb in Arp 299 was discovered by the ZTF survey, reported by Pignata et al. (2020), with an internal name ZTF18aarlpzd. The transient was first detected on 2020 March 28 06:19:45 UT at $m_g = 17.83 \pm 0.08$ mag with a reported non-detection on 2020 March 7 09:49:20 UT at $m_r = 19.34$ mag. The SN was classified by Tomasella et al. (2020) on 2020 April 2.8 UT as a young Type Ib, roughly a week before maximum, using the 1.82 m Copernico Telescope with the Asiago Faint Object Spectrograph and Camera (AFOSC). We obtained further optical spectrophotometric follow-up of SN 2020fkb using AFOSC, and the NOT with ALFOSC; optical imaging with the Asiago 67/92 cm Schmidt telescope with the KAF-16803 CCD; optical and near-IR imaging with the Liverpool Telescope (LT;

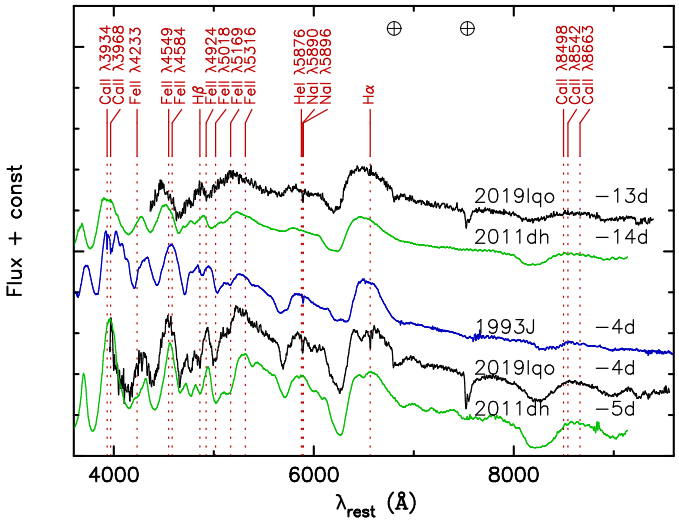

Fig. 12. Spectra of SN 2019lqo compared to those of Type IIb SNe 2011dh (Ergon et al. 2014) and 1993J (Matheson et al. 2000). The most prominent SN lines are indicated based on Ergon et al. (2014). The spectra have been extinction and redshift corrected, and shifted vertically for clarity. The main telluric band wavelengths for SN 2019lqo are indicated with a circled plus sign (⊕).

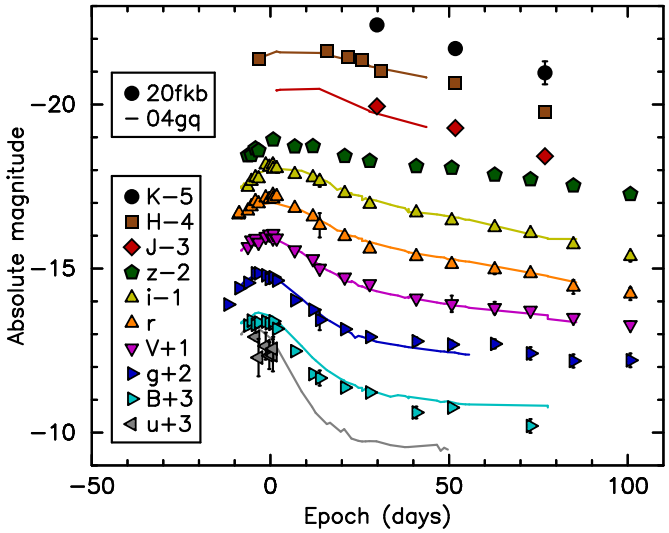

Fig. 13. SN 2020fkb absolute magnitude light curve (points) with an estimated host galaxy extinction of $A_V = 0.4$ mag yielded with a fit to Type Ib SN 2004gq, shown with solid lines and shifted vertically by +0.13 mag. The epoch 0 is set to the estimated V-band maximum.

Steele et al. 2004) using the IO:O and IO:I (Barnsley et al. 2016) instruments; and near-IR imaging using the NOT with NOTCam.

The standard reduction of the Asiago observatory data was carried out using the FOSCGUI pipeline[10], and basic instrumental pipeline reduction products of the LT data were obtained for the analysis. A selection of pre-explosion images were used as image subtraction templates from the NOT, the Asiago telescope, and the Pan-STARRS1 (Chambers et al. 2016) data release 2 archive[11]. The resulting PSF photometry of SN 2020fkb is listed in Tables A.8 and A.9.

The host galaxy extinction of SN 2020fkb was estimated using light curves of a normal Type Ib SN 2004gq (Bianco et al. 2014; Stritzinger et al. 2018a) with an excellent multi-band coverage and a low host galaxy extinction estimate of $A_V = 0.26$ mag (Stritzinger et al. 2018b). The fit suggests that SN 2020fkb peaked around JD = 2458949 ± 1 (i.e., around 2020 April 9), has a host galaxy extinction of $A_V = 0.4^{+0.1}_{-0.2}$ mag, and is $0.1^{+0.2}_{-0.1}$ mag fainter than SN 2004gq; the best match is shown in Fig. 13. For example, in r band SN 2020fkb peaked at $M_r \approx -17.2$ mag; this is not an unusual peak magnitude for a normal Type Ib SN, but is placed at the faint end of the r-band distribution of these SNe around −17 to −18 mag (e.g., Taddia et al. 2018). The pre-explosion non-detection limit, at an epoch corresponding to −33 d from maximum light, does not strongly constrain the explosion epoch of SN 2020fkb; normal Type Ib SNe have typical r-band rise times of ∼21 d (Taddia et al. 2015) with a distribution of a few days.

The spectral time series of SN 2020fkb (Table A.10) is shown in Fig. 14, compared to a selection of SN 2004gq spectra. The evolution of SN 2020fkb is quite normal for a Type Ib SN. The spectra show broad and evolving P Cygni profiles of He I features, in particular the $\lambda\lambda$5876, 6678, and 7065 lines. Furthermore, at pre-maximum the spectra show the Ca II H&K doublet, and broad features arising likely from Fe II blends. The He I λ5876 line Doppler velocity of the P Cygni absorption minimum close to light curve peak in our −4 d spectrum of SN 2020fkb is ∼9900 km s^{-1}; this is consistent with typical velocities of this feature at the corresponding phase of normal Type Ib SNe (Taddia et al. 2018), whereas the photometrically similar SN 2004gq actually shows overall larger velocities. The wavelength coverage of the +20 d spectrum onwards extends further redwards and the Ca II near-IR triplet is prominently visible. The +72 d spectrum is not completely nebular, but some nebular features have appeared; the doublets [O I] $\lambda\lambda$6300,6304 and [Ca II] $\lambda\lambda$7291,7324 are clearly present with a [O I]/[Ca II] flux ratio of ∼0.6. There is also strong indication of the [O I] λ5577 emission line; however, the Mg I] λ4571 feature seen in the nebular spectra of many normal Type Ib SNe (see e.g., Kuncarayakti et al. 2015) is not clearly present at this phase.

4. Starburst age in high CCSN rate LIRGs

The numerous CCSN subtypes are expected to originate from different populations of massive stars that have differences, for example in their life times. Motivated by this, we modelled the basic starburst parameters in all LIRGs that have hosted nuclear CCSNe to investigate whether there is a trend between CCSN subtypes and starburst age, t_{SB}. Our SN sample comprises the classified CCSNe in LIRGs at small projected distances from the host nucleus that are listed in Kool et al. (2018) and Kool (2019), and expanded by the new events presented in this manuscript. The sample events are discovered either at optical or IR wavelengths; we do not consider in our sample SN candidates detected only in radio. In addition to the new CCSNe in NGC 3256 and Arp 299, we also included in our analysis the recent Type II SN 2020cuj in NGC 1614 that has a limited data set (see Appendix A). As the star formation in LIRGs is heavily concentrated in the nuclear regions ranging in size from ∼100 to ∼1000 pc (e.g., Soifer et al. 2001), the contribution of this region to the total CCSN rate is typically >50%. For example, two-thirds of the young massive clusters in the LIRG Arp 299-A reside within ∼2.2 kpc of the nuclear regions (Randriamanakoto et al. 2019). Furthermore, the panchromatic luminosity of these galaxies is dominated by their

[10] https://sngroup.oapd.inaf.it/foscgui.html
[11] https://panstarrs.stsci.edu/

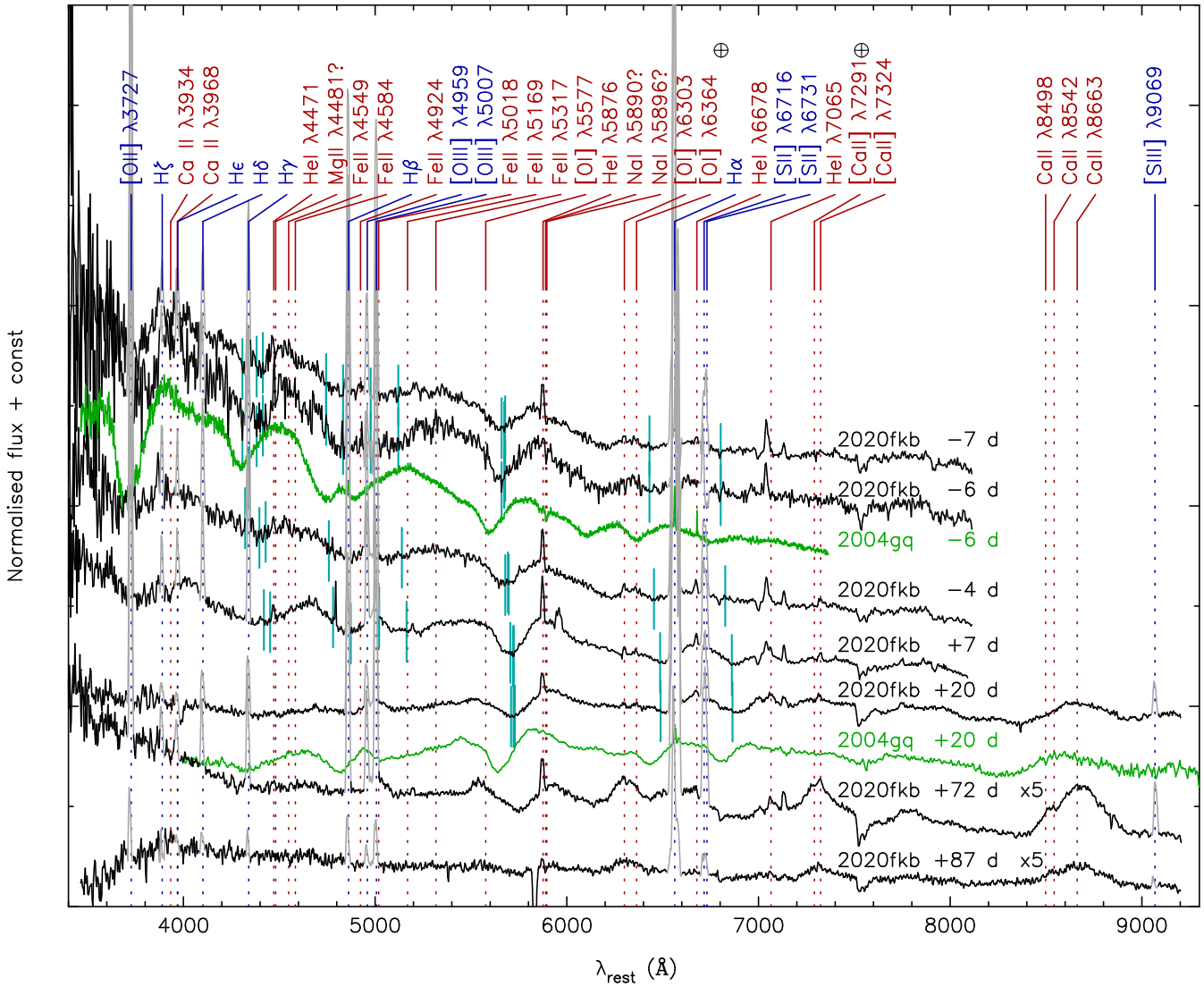

Fig. 14. Spectral time series of SN 2020fkb redshift corrected to rest frame. The spectra have been corrected for both Galactic and estimated host galaxy extinctions, and vertically shifted and normalised for clarity. The epochs are provided respective to the estimated light curve maximum. The most prominent spectral features are labelled coming either from the host galaxy (blue) or from the SN (red). The Doppler shifted positions of the He I and Fe II lines are indicated with cyan vertical lines in early epochs as suggested by the velocity of the He I λ5876 absorption minimum. The most prominent narrow host emission features are shown in grey, and the telluric band wavelengths with a circled plus sign (⊕). The spectra of SN 2020fkb likely contain some host continuum contamination at the blue end, in particular in the late epochs. Selected spectra of normal Type Ib SN 2004gq (Modjaz et al. 2014) are shown for comparison (green), and show very similar spectrophotometric evolution, but somewhat larger line velocities.

central regions. While the SED fitting of the LIRGs is carried out here for the whole galaxy (largely due to the limitations of the available photometry), the luminosity and star formation characteristics are nonetheless dominated by the central regions of these systems. We set the CCSN sample limit conservatively at ≤2.5 kpc projected distance limit from the centres of their host galaxies. Our initial sample thus consists of 16 LIRGs ($18 \leq D_{\rm l} \leq 150$ Mpc) and 29 SNe (12 II, 3 IIn, 13 IIb/Ib/Ic, and 1 Ibn). We modelled the SEDs of these sample LIRGs to study the distribution of the CCSN subtypes and the host starburst age in these galaxies. We note that we were not able to model the nearby and extended IC 2163/NGC 2207 system (host of SPIRITS 14buu and SPIRITS 15c; Jencson et al. 2017) due to the vastly differing spatial coverage across the range of wavelengths we considered; thus, this LIRG is not part of our sample. Furthermore, we did not include Type II SN 2004gh (Folatelli et al. 2004) in our analysis as the SED of its host galaxy MCG -04-25-06 has a very limited wavelength coverage available, which would not enable robust modelling.

It is possible that due to chance alignment some of the CCSNe with small projected distances are in fact located at much larger distances from the host nucleus. While this cannot be accurately constrained, the host galaxy extinction provides a hint of the true location of the CCSNe in LIRGs; CCSNe that are more obscured by host galaxy extinction are also more likely to be embedded in the dusty central regions of their hosts. This is a strong motivation to estimate host galaxy extinctions for CCSNe in LIRGs, as we have done for the new events presented in this paper. The sample CCSNe are listed in Table 1 with the available reported host galaxy extinctions.

We used a grid of radiative transfer models for a starburst (Efstathiou et al. 2000; Efstathiou & Siebenmorgen 2009), AGN (Efstathiou & Rowan-Robinson 1995; Efstathiou et al. 2013), and a spheroidal galaxy (Efstathiou et al. 2021) or a disc galaxy

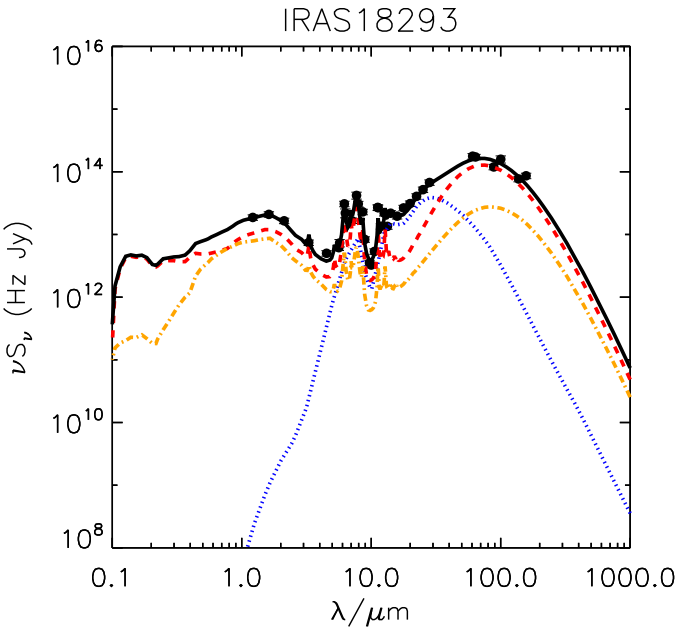

Fig. 15. Example SED fit (solid black curve) to the data of one of the sample LIRGs, IRAS 18293−3413 (points), with a combination of a starburst (dashed red), a spheroidal galaxy (dot-dashed orange), and an AGN (dotted blue) component.

(Efstathiou & Siebenmorgen, in prep.) to fit the SEDs using the SED Analysis Through Markov Chains (SATMC) Monte Carlo code (Johnson et al. 2013). The host galaxy model resulting for the best fit is indicated in Table 1. The starburst and host galaxy models incorporate the stellar population synthesis model of Bruzual & Charlot (1993, 2003) and assume a solar metallicity and a Salpeter initial mass function (IMF). Alonso-Herrero et al. (2006) studied a local sample of LIRGs and found them to have approximately solar metallicity. While adopting a different IMF can have some effect on the derived parameters (see discussion in Herrero-Illana et al. 2017), we adopt the classical Salpeter IMF, consistently with previous studies. The fitting predicts the starburst SED at different ages with the assumption that the star formation rate declines exponentially. The spheroidal galaxy model used here is an evolution of the cirrus model of Efstathiou & Rowan-Robinson (2003) and is similar to that of Silva et al. (1998), incorporated in the GRAphite and SILicate (GRASIL) code. The model assumes that stars, dust, and molecular clouds in which young stars are embedded are mixed in a spherical cloud with a Sersic profile with index $n = 4$. The method for computing the disc model is similar to that used for the spheroidal models, apart from the difference in the geometry. The SATMC fitting includes 13 and 14 free parameters for the spherical and the disc models, respectively. The degrees of freedom (DOFs) for the best fit are indicated in Table 1. The SATMC derives errors for the fitting parameters, which Johnson et al. state to be the 68% contained ranges from the one-dimensional confidence levels, marginalised over the other fitting parameters.

For the SED fitting we collated the optical to far-IR photometric data of the sample LIRGs via the NASA/IPAC Extragalactic Database[12] (NED) mainly from the Galaxy Evolution Explorer (GALEX), SDSS, 2MASS, the Infrared Astronomical Satellite (IRAS), and the Infrared Space Observatory (ISO). We also used photometric data obtained with the *Herschel* Space Observatory from Chu et al. (2017).

[12] http://ned.ipac.caltech.edu/

For three LIRGs (IC 883, IRAS 17138−1017, and IRAS 18293−3413) the *Spitzer* spectra used by Herrero-Illana et al. (2017) for their modelling were also used for the reanalysis here. For five additional LIRGs in our sample (ESO 138−G27, NGC 1614, NGC 2388, NGC 317B, and NGC 838) low-resolution ($R \approx 60-127$) mid-IR spectra were available from the short-low (SL; 5.2−14.5 μm) and long-low (LL; 14−38 μm) modules of the Infrared Spectrograph (IRS; Houck et al. 2004) on board the *Spitzer* Space Telescope. For observations that were carried out in mapping mode, we only selected those frames where the spectrograph slit included the nucleus of the galaxy. The data were processed using standard spectroscopic techniques. We began by subtracting one nod position from the other to remove the sky background. All subsequent steps (extraction, wavelength calibration, and flux calibration) were carried out using the optimal extraction mode of the *Spitzer* IRS Custom Extractor (SPICE) tool (v2.5.1). The absolute flux calibration was checked against the photometric data. In the case of nearby LIRGs (<50 Mpc) we decided not to use IRS data as the field of view of IRS is much smaller than the angular size of the galaxies. The IRS spectra were binned to steps of $\log_{10}(\lambda_{\rm rest}/\mu{\rm m}) = 0.05$ to match more closely the resolution of the radiative transfer models; a more relaxed match was applied around the complex regions of the polycyclic aromatic hydrocarbon (PAH) and the 9.7 μm silicate features. For each sample LIRG three sets of Monte Carlo fits were carried out for the spheroidal and disc galaxy model cases, and the individual fit with the best reduced χ^2 value was adopted to yield the starburst parameters for the system. Our global estimates of the CCSN rate and starburst properties of the sample galaxies are reported in Table 1 and an example SED fit of IRAS 18293−3413 is shown in Fig. 15. The best SED fits for all the other sample galaxies are shown in Figs. A.3 and A.4. We note that the LIRG sample partly overlaps that of Herrero-Illana et al. (2017), with some differences in the yielded starburst values obtained via similar simulations. The key differences are the more extended parameter ranges allowed in our simulations for the starburst age (5–50 Myr) and the *e*-folding time of the starburst (1–40 Myr). While preparing this study we found that the starburst age range used in the simulations of Herrero-Illana et al., which had an upper limit of 29.5 Myr, resulted in many of their older starburst age estimates to artificially cluster near this value. However, the starburst age was not the focus of that study and does not change their conclusions. Similarly any differences in the derived parameters previously reported by Mattila et al. (2012) and Mattila et al. (2018) result from using different data sets for their SED fitting covering separately individual components of Arp 299 with a more limited wavelength range rather than fitting the SED of the whole system. Thus, the results for the starburst age are not directly comparable.

Figure 16 shows our result with the host LIRG starburst age comparison to the projected distance of the CCSN, with the different CCSN subtypes highlighted. Due to the still relatively small number of discovered CCSNe in LIRGs, we combined Type IIb, Ib, and Ic SNe into a single group of H-poor IIb/Ib/Ic events. We see that the H-rich CCSNe around the central regions of these galaxies are produced in LIRGs with older starburst ages (≥30 Myr), while the H-poor CCSNe are produced primarily in younger starburst age regions. This is consistent with canonical stellar evolution models. In younger starbursts only the most massive stars have had time to evolve to the SN phase, and explode as H-poor CCSNe; in the older starbursts the most massive stars have already exploded, and the lower mass stars

Table 1. Confirmed and likely CCSNe at the central regions ($d_{\rm proj} \leq 2.5$ kpc) of LIRGs with SED model based global star formation properties of LIRG hosts (see compilations of Kool et al. 2018; Kool 2019, and references therein).

Host	$D_{\rm l}$ (Mpc)	$\log(L_{\rm IR})$ ($L_\odot$)	$t_{\rm SB}$ (Myr)	$SNR_{\rm SB}$ (SN yr^{-1})	SFR ($M_\odot$ yr^{-1})	$L_{\rm AGN}$ (%)	SED host	DOF	CCSN	Type	$d_{\rm proj}$ (kpc)	$A_V^{\rm host}$ (mag)	Disc.	Ref.
IRAS 18293−3413	84.1	11.89	40^{+1}_{-5}	$2.3^{+0.4}_{-0.2}$	275^{+50}_{-42}	49^{+13}_{-9}	S	22	AT 2012iz	IIP	0.6	1.8	IR	(1)
IRAS 18293−3413	...	...	...	...	...	...	...	...	SN 2013if	IIP	0.2	0	IR	(2)
IC 883	107.1	11.73	38^{+1}_{-1}	$2.1^{+0.1}_{-0.1}$	233^{+21}_{-17}	45^{+13}_{-20}	D	27	SN 2010cu	IIP	0.2	0	IR	(3)
IC 883	...	...	...	...	...	...	...	...	SN 2011hi	IIP	0.4	6	IR	(3)
NGC 5331	150.0	11.66	35^{+1}_{-3}	$1.8^{+0.2}_{-0.3}$	212^{+19}_{-39}	21^{+4}_{-5}	D	5	AT 2017chi	IIn	1.5	12	IR	(1)
Arp 299	44.8	11.82	16^{+2}_{-4}	$1.5^{+0.1}_{-0.2}$	99^{+9}_{-16}	0.0	S	5	SN 1998T	Ib	1.5	?	Opt	(4)
Arp 299	...	...	...	...	...	...	...	...	SN 2005U	IIb	1.4	?	IR	(4)
Arp 299	...	...	...	...	...	...	...	...	SN 2010O	Ib	1.2	1.9	Opt	(5)
Arp 299	...	...	...	...	...	...	...	...	SN 2010P	IIb	0.2	7	IR	(5)
Arp 299	...	...	...	...	...	...	...	...	SN 2019lqo	IIb	2.0	2.1	Opt	(6)
Arp 299	...	...	...	...	...	...	...	...	SN 2020fkb	Ib	0.7	0.4	Opt	(6)
NGC 1614	66.8	11.66	25^{+2}_{-1}	$1.1^{+0.1}_{-0.1}$	94^{+11}_{-3}	61^{+4}_{-4}	S	33	SN 1996D	Ic	2.1	?	Opt	(2)
NGC 1614	...	...	...	...	...	...	...	...	SN 2020cuj	II	2.5	2.8	Opt	(5)
NGC 838	53.3	11.05	25^{+2}_{-1}	$1.0^{+0.1}_{-0.1}$	90^{+8}_{-7}	30^{+30}_{-9}	S	7	SN 2005H	II	0.4	?	Opt	(2)
IRAS 17138−1017	82.2	11.49	28^{+7}_{-1}	$0.8^{+0.1}_{-0.1}$	69^{+37}_{-4}	31^{+20}_{-4}	S	22	SN 2008cs	IIn	1.5	16	IR	(7)
IRAS 17138−1017	...	...	...	...	...	...	...	...	SN 2015cb	IIP	0.6	4.6	IR	(2)
NGC 2388	61.1	11.28	25^{+1}_{-1}	$0.7^{+0.1}_{-0.1}$	63^{+5}_{-3}	37^{+3}_{-2}	D	8	SN 2015U	Ibn	1.8	3.1	Opt	(8)
NGC 317B	77.0	11.19	37^{+1}_{-1}	$0.7^{+0.1}_{-0.1}$	73^{+2}_{-4}	45^{+4}_{-3}	S	30	SN 1999gl	II	1.9	?	Opt	(2)
NGC 317B	...	...	...	...	...	...	...	...	SN 2014dj	Ic	1.5	?	Opt	(2)
NGC 3256	37.4	11.61	43^{+1}_{-4}	$0.6^{+0.1}_{-0.1}$	64^{+8}_{-14}	37^{+4}_{-2}	S	16	SN 2001db	II	2.1	5.5	IR	(6)
NGC 3256	...	...	...	...	...	...	...	...	PSN102750	IIn	2.1	0.3	Opt	(6)
NGC 3256	...	...	...	...	...	...	...	...	SN 2018ec	Ic	1.7	2.1	IR	(6)
NGC 3256	...	...	...	...	...	...	...	...	AT 2018cux	IIP	0.8	2.1	Opt	(6)
ESO 138−G27	96.1	11.41	31^{+2}_{-2}	$0.6^{+0.1}_{-0.1}$	60^{+6}_{-10}	46^{+2}_{-3}	S	27	SN 2009ap	Ic	1.2	?	Opt	(2)
NGC 6907	49.2	11.11	39^{+1}_{-2}	$0.6^{+0.1}_{-0.2}$	79^{+13}_{-25}	45^{+4}_{-6}	S	2	SN 2008fq	II	1.4	?	Opt	(2)
NGC 2146	18.0	11.15	30^{+2}_{-1}	$0.3^{+0.1}_{-0.1}$	33^{+3}_{-2}	82^{+3}_{-3}	S	8	SN 2005V	Ib/c	0.5	?	IR	(2)
MCG -02-01-052	115.2	11.48	41^{+4}_{-3}	$0.1^{+0.1}_{-0.1}$	18^{+12}_{-7}	58^{+20}_{-22}	S	3	SN 2010hp	II	2.1	0.5	IR	(9)
NGC 6000	28.1	10.95	11^{+6}_{-2}	$0.1^{+0.1}_{-0.1}$	7^{+5}_{-3}	32^{+3}_{-3}	S	4	SN 2010as	IIb	0.6	1.8	Opt	(10)
NGC 5433	70.3	11.01	46^{+2}_{-11}	<0.03	24^{+2}_{-1}	25^{+19}_{-5}	S	2	SN 2010gk	Ic	2.0	?	Opt	(2)

Notes. Luminosity distances are obtained via NED. References for the CCSNe and their host galaxy extinction estimates, if available, are given in brackets.
References. 1) Kool (2019), 2) Kool et al. (2018), 3) Kankare et al. (2012), 4) Mattila et al. (2012), 5) Kankare et al. (2014a), 6) This work, 7) Kankare et al. (2008), 8) Pastorello et al. (2015), 9) Miluzio et al. (2013), 10) Folatelli et al. (2014).

have had more time to evolve to the SN stage and end their life cycles as H-rich CCSNe (e.g., Heger et al. 2003). However, rotation, metallicity, and binarity (e.g., Podsiadlowski et al. 1992; Woosley 2019) all have an influence on this, and can reduce the relative initial progenitor star mass and life time differences between different CCSN subtypes.

We carried out a two-sample Anderson-Darling (AD) statistical test for the CCSN subtype distribution. The p-value for the two basic CCSN subtypes of H-poor Type IIb/Ib/Ic/Ibn (14 SNe) and H-rich Type II/IIn (15 SNe) in these galaxies having the same underlying distribution is only 0.0027, and thus the discussed trend is statistically significant at the 3.0σ level. We also considered the case of only the LIRGs with the highest yielded SN rates of $\geq$0.5 CCSN yr^{-1}. Then the p-value of the two basic CCSN subtypes having the same underlying distribution is reduced to 0.0013 (3.2σ). We chose the AD test over other empirical distribution statistics-based tests (e.g., a Kolmogorov–Smirnov test) because of its generally powerful ability to distinguish between distributions that have the largest differences near the minima and maxima of their cumulative distribution (Stephens 1974). As an additional AD test, we also compared our SN samples to a 'flat' larger simulated comparison sample of a sufficiently large number (10) of SNe distributed uniformly in each of the corresponding sample galaxies. The resulting p-value for the Type IIb/Ib/Ic/Ibn SNe being uniformly distributed among these galaxies is 0.011 (2.5σ). However, for the $SNR \geq 0.5$ CCSN yr^{-1} sample the p-value is reduced to 0.00060 (3.4σ). Type II/IIn SNe are consistent with the uniform distribution in these comparisons with a p-value of 0.14 (1.5σ) and 0.075 (1.8σ) for the $\geq$0.0 and $\geq$0.5 CCSN yr^{-1} samples, respectively. Furthermore, we also consider cases with the sample groups defined as Type II and Type IIb/Ib/Ic SNe. Generally, these groups with reduced statistics appear to slightly increase the p-values. The full presentation of the yielded values are listed in Table 2. The p-values for the estimated probabilities of obtaining a difference that is at least as extreme as that seen in the comparisons were converted to the corresponding standard deviation (σ) units z of a half-normal distribution

by solving $p/2 = (2\pi)^{-1/2} \int_z^\infty (e^{-x^2/2})dx$. A half-normal distribution is warranted as the AD test probes the absolute difference $|t_{SB,1} - t_{SB,2}|$ between distributions. We note that there is no standard method for taking the data point errors into account with the AD statistical test (or other similar tests).

The obvious caveat of these trends is that the results are based on a relatively small sample of only 29 CCSNe and their 16 host LIRGs. Furthermore, the model dependencies and errors associated with the starburst age estimations are not taken into account in the significance calculations. This is a strong motivation to discover and study more CCSNe in the central regions of LIRGs to improve sample statistics. Removing an individual galaxy from the studied samples, and thus typically one or two CCSNe, will not result in major differences in the yielded p-values. However, arbitrarily removing Arp 299 from the sample, and therefore six Type IIb/Ib SNe from the analysed samples, would result in the disappearance of the discussed trends (see Fig. 17). For completeness, jackknife resampling averages of the p-values are also listed in Table 2 with the corresponding values of standard error of the mean.

Our assumption was that very high CCSN rate LIRGs can have effectively dominating starburst episodes that produce the majority of CCSNe in these galaxies. However, even if these galaxies had one recent dominating starburst episode, this would not quench the underlying and ongoing star formation and CCSN production on a lower efficiency. Similarly, the sample LIRGs could also have other more minor non-dominating starburst episodes. Therefore, these galaxies can still produce any SN subtypes, though at a more moderate rate and, on average, less concentrated towards the central regions of their hosts.

The starburst ages ranging from ∼25 to 40 Myr, as found for LIRGs hosting primarily H-rich SNe in our sample, correspond to progenitor lifetimes for zero age main sequence (ZAMS) mass M_{ZAMS} of ∼11–8 $M_\odot$, according to the Geneva group single-star stellar evolution tracks in solar metallicity with rotation (Ekström et al. 2012). This is consistent with theory and with the direct red supergiant (RSG) progenitor detections of nearby Type IIP SNe (Smartt 2009). Similarly, our estimate of the global starburst age of 16^{+2}_{-4} Myr for Arp 299 corresponds to progenitor masses of roughly 13–18 $M_\odot$ (Ekström et al. 2012). Intriguingly, the progenitors of many canonical Type IIb SNe are typically found within this range of initial mass, and in a binary system, for example 1993J (Nomoto et al. 1993; Podsiadlowski et al. 1993; Aldering et al. 1994; Woosley et al. 1994), 2008ax (Crockett et al. 2008; Folatelli et al. 2015), 2011dh (Maund et al. 2011; Van Dyk et al. 2011; Ergon et al. 2014), 2013df (Morales-Garoffolo et al. 2014; Van Dyk et al. 2014), and 2016gkg (Bersten et al. 2018). From our sample of six central CCSNe in Arp 299, 50% are Type IIb and 50% are Type Ib events. Kangas et al. (2017) found consistent Hα associations between Type IIb SNe and $M_{ZAMS} \sim 15\,M_\odot$ yellow super giants, and Type Ib SNe and $M_{ZAMS} \sim 15\,M_\odot$ RSGs. Here we find results consistent with those above, and note the advantage of using LIRGs (in comparison to normal spiral galaxies) for statistical studies as the starburst age can be more strictly constrained in these galaxies.

Anderson et al. (2011) and Anderson & Soto (2013) highlight the tendency of the Arp 299 system to produce Type Ib to Type IIb SNe, compared to their normal fraction of all CCSNe in the local Universe. This relative excess is thought to rise either from the young age of the recent star formation or from a top-heavy IMF (Anderson et al. 2011). The recent SNe 2019lqo and 2020fkb follow the trend of Type Ib/IIb SNe in Arp 299, which we argue is consistent with the dominating episode of recent star formation with a normal (Salpeter) IMF adopted. Pérez-Torres et al. (2009) reported the radio detection of 20 SNe or SN remnants within the <150 pc nuclear region of the nucleus of Arp 299-A, including three young radio SNe. They concluded that the properties of the young SNe are consistent with those of either Type IIb or normal Type II SNe. If Arp 299 produces predominantly Type Ib/IIb SNe, this suggests that these recent SNe are predominantly Type IIb SNe. For comparison, Alonso-Herrero et al. (2000) inferred a starburst age of ∼11 Myr for the Arp 299-A component that dominates the star formation in the Arp 299 system. Within errors, this is consistent with our global estimate for this LIRG. For the other less dominating

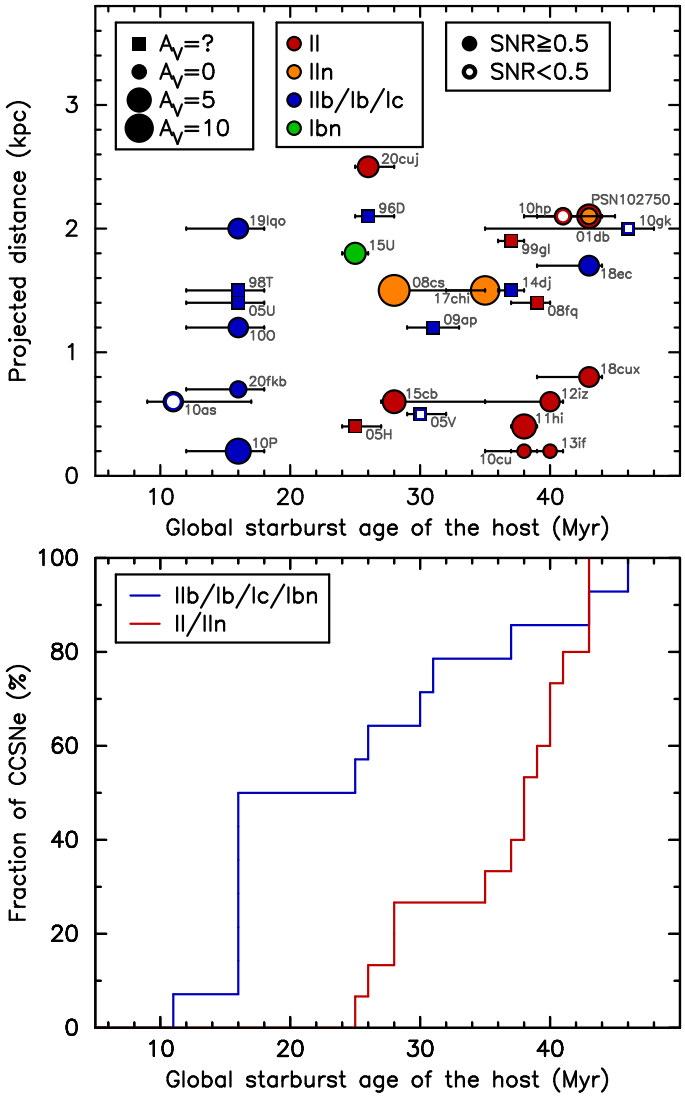

Fig. 16. Comparison between the starburst age and the CCSN subtype. *Upper panel*: type distribution of classified CCSNe compared to our SED modelled global age of the host starburst at the central regions of our sample LIRGs. Host galaxy extinctions of the SNe are indicated by the sizes of the circles; unknown (and likely small) extinction cases are indicated by squares. The symbol colours indicate the CCSN subtype classifications. The events are indicated with closed and open symbols based on their estimated host CCSN rate above and below 0.5 CCSN yr^{-1}, respectively. *Lower panel*: simplified cumulative distribution presentation of the upper panel data of the Type IIb/Ib/Ic/Ibn and Type II/IIn samples of CCSNe. The data suggests that H-poor and H-rich CCSNe come from very young ($\lesssim$30 Myr) and older ($\gtrsim$30 Myr) starbursts, respectively.

Table 2. AD statistical test results of p-values and corresponding standard deviation (σ) units for our CCSN samples having the same underlying distributions of estimated global starburst age of the host.

	$SNR \geq 0.0$				$SNR \geq 0.5$			
	p-value	σ	$\theta_{p\text{-value}}$	θ_σ	p-value	σ	$\theta_{p\text{-value}}$	θ_σ
IIb/Ib/Ic/Ibn vs. II/IIn	0.0027	3.0	0.017 ± 0.014	$2.4^{+0.6}_{-0.2}$	0.0013	3.2	0.040 ± 0.038	$2.1^{+1.0}_{-0.3}$
IIb/Ib/Ic vs. II/IIn	0.0039	2.9	0.030 ± 0.025	$2.2^{+0.6}_{-0.3}$	0.0017	3.1	0.078 ± 0.076	$1.8^{+1.3}_{-0.4}$
IIb/Ib/Ic vs. II	0.0059	2.8	0.032 ± 0.025	$2.1^{+0.6}_{-0.2}$	0.0035	2.9	0.083 ± 0.078	$1.7^{+1.1}_{-0.3}$
IIb/Ib/Ic/Ibn vs. $\text{flat}_{\text{IIb/Ib/Ic/Ibn/II/IIn}}$	0.011	2.5	0.058 ± 0.046	$1.9^{+0.6}_{-0.3}$	0.00060	3.4	0.070 ± 0.069	$1.8^{+1.5}_{-1.5}$
IIb/Ib/Ic vs. $\text{flat}_{\text{IIb/Ib/Ic/II/IIn}}$	0.015	2.4	0.071 ± 0.054	$1.8^{+0.6}_{-0.3}$	0.00072	3.4	0.089 ± 0.088	$1.7^{+1.6}_{-0.3}$
IIb/Ib/Ic vs. $\text{flat}_{\text{IIb/Ib/Ic/II}}$	0.022	2.3	0.083 ± 0.060	$1.7^{+0.6}_{-0.2}$	0.0011	3.3	0.094 ± 0.093	$1.7^{+1.6}_{-0.4}$
II/IIn vs. $\text{flat}_{\text{IIb/Ib/Ic/Ibn/II/IIn}}$	0.14	1.5	0.16 ± 0.02	$1.4^{+0.1}_{-0.1}$	0.075	1.8	0.10 ± 0.02	$1.6^{+0.2}_{-0.1}$
II/IIn vs. $\text{flat}_{\text{IIb/Ib/Ic/II/IIn}}$	0.24	1.2	0.27 ± 0.03	$1.1^{+0.1}_{-0.1}$	0.15	1.4	0.20 ± 0.03	$1.3^{+0.1}_{-0.1}$
II vs. $\text{flat}_{\text{IIb/Ib/Ic/II}}$	0.28	1.1	0.32 ± 0.03	$1.0^{+0.1}_{-0.1}$	0.24	1.2	0.29 ± 0.03	$1.1^{+0.1}_{-0.1}$

Notes. Additional tests include comparisons to a 'flat' simulated sample, including galaxies that have hosted ≥1 CCSN from a selection of indicated types. Two CCSN rate ranges are considered. For completeness, the table also lists the jackknife resampling mean ($\theta_{p\text{-value}}$) and standard error values, and the corresponding σ units (θ_σ), which are dominated by the arbitrary removal of Arp 299 and its CCSNe from the samples.

nuclei (B, C, C′) they find indications of a somewhat younger starburst age, in particular in nuclei C′ and C of ∼4 and 5 Myr, respectively; this implies that only very massive stars in the ∼50–90 $M_\odot$ range are expected to explode as CCSNe. For a Salpeter IMF, the fraction of such massive stars is fairly insignificant, and thus the most recent star formation episode could not have contributed significantly to the observed CCSN rate and population in Arp 299.

5. Conclusions

We discovered a new Type Ic SN 2018ec in the LIRG NGC 3256 during the ESO science verification run of the adaptive optics seeing enhancer instrument HAWK-I/GRAAL. While carrying out a follow-up of this SN, we discovered another transient, AT 2018cux, in the same galaxy that was a subluminous Type IIP SN. We derive the host galaxy extinctions of $A_V = 2.1^{+0.3}_{-0.1}$ and 2.1 ± 0.4 mag for SN 2018ec and AT 2018cux, respectively. A SN candidate from 2014, PSN102750, in the same galaxy was found to be consistent with H-rich CCSN with a fairly low host galaxy extinction. The best fit for PSN102750 is provided by a Type IIn using a combination of early ground-based follow-up and late-time colours from HST; however, we cannot fully rule out a Type IIP origin. We also report a follow-up of Type IIb SN 2019lqo and Type Ib SN 2020fkb in Arp 299 and derive a line-of-sight host extinction of $A_V = 2.1^{+0.1}_{-0.3}$ and $0.4^{+0.1}_{-0.2}$ mag for them, respectively.

We find evidence that the CCSN subtypes occurring within ∼2.5 kpc of the nucleus of LIRGs correlate with the inferred starburst age of the host and are consistent with a normal (Salpeter) IMF. In other words, the H-rich (Type II/IIn) and H-poor (Type IIb/Ib/Ic/Ibn) CCSN progenitors have different underlying age distributions in these galaxies at a 3σ significance level. However, the overall trend was drawn from a relatively small sample size of CCSNe and their host galaxies, and the significance comparisons between subgroups do not specifically take into account error ranges of the yielded starburst ages. Hence, future surveys, in particular in high spatial resolution IR, will be necessary to discover and further study CCSNe in LIRGs.

We predict, that LIRGs that have hosted multiple discovered circumnuclear CCSNe in their central regions will continue to predominantly produce the subtypes that they have already shown to favour in their nuclear regions. New CCSN discoveries in these galaxies will constrain more accurately a typical projected distance limit for this trend, or alternatively a possible effective radius limit that should be adopted. At the moment, the very small number statistics of the currently available sample of SNe in these galaxies do not allow for more sophisticated constraints. Furthermore, with improved statistics, the discussed

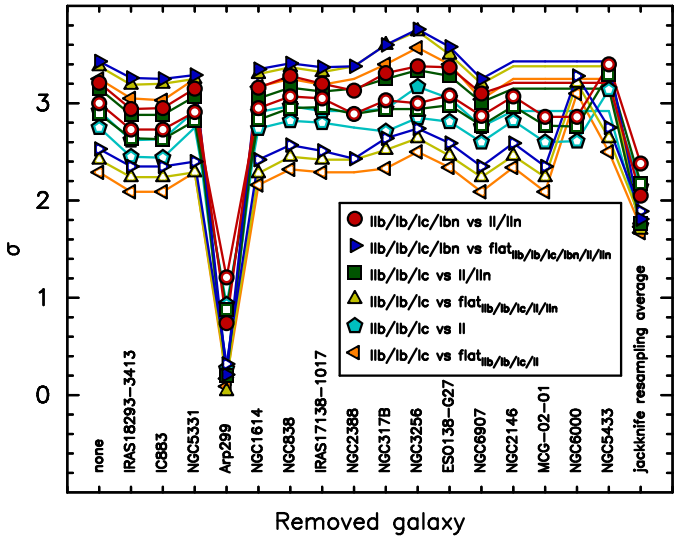

Fig. 17. Sigma values from a selection of statistical tests for the sample with individual galaxies and their sample CCSNe removed from the analysis as a test. While removing individual galaxies from the sample, and thus typically only one or two CCSNe, will not have a major effect on the resulting AD test values, the arbitrary removal of Arp 299 and its 6 Type IIb/Ib SNe would make the discussed trends non-existent. Open and closed symbols show the values for samples with the host SNR of ≥0.0 and ≥0.5 CCSN yr^{-1}, respectively. Data points are not shown in cases where the removal of the galaxy is irrelevant for the comparison between the analysed samples. With the large number of hosted sample CCSNe, the removal of the LIRG Arp 299 with a yielded young starburst age also has the largest weight in the jackknife resampling averages of the p-values for each set of comparisons, and result in mean values of $\theta_p \geq 0.017$ ($\leq 2.4\sigma$).

trend offers a possible new method to probe the progenitor systems of different CCSN types by using high-IR-luminosity LIRGs as laboratories.

Acknowledgements. We thank the anonymous referee for useful comments. We thank Marco Fiaschi for carrying out some of the Asiago observations. EK is supported by the Turku Collegium of Science, Medicine and Technology. EK also acknowledge support from the Science and Technology Facilities Council (STFC; ST/P000312/1). ECK acknowledges support from the G.R.E.A.T. research environment and support from The Wenner-Gren Foundations. MF is supported by a Royal Society – Science Foundation Ireland University Research Fellowship. EC, LT, AP, and MT are partially supported by the PRIN-INAF 2017 with the project "Towards the SKA and CTA era: discovery, localization, and physics of transient objects". HK was funded by the Academy of Finland projects 324504 and 328898. TWC acknowledges the EU Funding under Marie Skłodowska-Curie grant agreement No. 842471. LG was funded by the European Union's Horizon 2020 research and innovation programme under the Marie Skłodowska-Curie grant agreement No. 839090. This work has been partially supported by the Spanish grant PGC2018-095317-B-C21 within the European Funds for Regional Development (FEDER). MG is supported by the Polish NCN MAESTRO grant 2014/14/A/ST9/00121. KM acknowledges support from EU H2020 ERC grant no. 758638. TMB was funded by the CONICYT PFCHA / DOCTORADOBECAS CHILE/2017-72180113. MN is supported by a Royal Astronomical Society Research Fellowship. Based on observations collected at the European Organisation for Astronomical Research in the Southern Hemisphere under ESO programmes 67.D-0438, 60.A-9475, 199.D-0143, and 1103.D-0328. Some of the observations reported in this paper were obtained with the Southern African Large Telescope (SALT) under programme 2018-1-DDT-003 (PI: Kankare). Polish participation in SALT is funded by grant No. MNiSW DIR/WK/2016/07. Based on observations made with the Nordic Optical Telescope, operated by the Nordic Optical Telescope Scientific Association at the Observatorio del Roque de los Muchachos, La Palma, Spain, of the Instituto de Astrofisica de Canarias. The data presented here were obtained in part with ALFOSC, which is provided by the Instituto de Astrofisica de Andalucia (IAA) under a joint agreement with the University of Copenhagen and NOTSA. This work is partly based on the NUTS2 programme carried out at the NOT. NUTS2 is funded in part by the Instrument Center for Danish Astrophysics (IDA). The Liverpool Telescope is operated on the island of La Palma by Liverpool John Moores University in the Spanish Observatorio del Roque de los Muchachos of the Instituto de Astrofisica de Canarias with financial support from the UK Science and Technology Facilities Council. This paper is also based on observations collected at the Copernico 1.82 m and Schmidt 67/92 Telescopes operated by INAF – Osservatorio Astronomico di Padova at Asiago, Italy. Based on observations obtained at the Gemini Observatory, which is operated by the Association of Universities for Research in Astronomy, Inc., under a cooperative agreement with the NSF on behalf of the Gemini partnership: the National Science Foundation (United States), the National Research Council (Canada), CONICYT (Chile), Ministerio de Ciencia, Tecnología e Innovación Productiva (Argentina), and Ministério da Ciência, Tecnologia e Inovação (Brazil). Observations were carried out under programme GS-2017A-C-1. This project used data obtained with the Dark Energy Camera (DECam), which was constructed by the Dark Energy Survey (DES) collaboration. Funding for the DES Projects has been provided by the DOE and NSF (USA), MISE (Spain), STFC (UK), HEFCE (UK), NCSA (UIUC), KICP (U. Chicago), CCAPP (Ohio State), MIFPA (Texas A&M University), CNPQ, FAPERJ, FINEP (Brazil), MINECO (Spain), DFG (Germany) and the collaborating institutions in the Dark Energy Survey, which are Argonne Lab, UC Santa Cruz, University of Cambridge, CIEMAT-Madrid, University of Chicago, University College London, DES-Brazil Consortium, University of Edinburgh, ETH Zürich, Fermilab, University of Illinois, ICE (IEEC-CSIC), IFAE Barcelona, Lawrence Berkeley Lab, LMU München and the associated Excellence Cluster Universe, University of Michigan, NOAO, University of Nottingham, Ohio State University, OzDES Membership Consortium, University of Pennsylvania, University of Portsmouth, SLAC National Lab, Stanford University, University of Sussex, and Texas A&M University. Based on observations obtained with the Samuel Oschin 48-inch Telescope at the Palomar Observatory as part of the Zwicky Transient Facility project. ZTF is supported by the National Science Foundation under Grant No. AST-1440341 and a collaboration including Caltech, IPAC, the Weizmann Institute for Science, the Oskar Klein Center at Stockholm University, the University of Maryland, the University of Washington, Deutsches Elektronen-Synchrotron and Humboldt University, Los Alamos National Laboratories, the TANGO Consortium of Taiwan, the University of Wisconsin at Milwaukee, and Lawrence Berkeley National Laboratories. Operations are conducted by COO, IPAC, and UW. Based on observations at Cerro Tololo Inter-American Observatory, National Optical Astronomy Observatory (NOAO Prop. ID 2017A-0260; and PI: Soares-Santos), which is operated by the Association of Universities for Research in Astronomy (AURA) under a cooperative agreement with the National Science Foundation. The Pan-STARRS1 Surveys (PS1) and the PS1 public science archive have been made possible through contributions by the Institute for Astronomy, the University of Hawaii, the Pan-STARRS Project Office, the Max-Planck Society and its participating institutes, the Max Planck Institute for Astronomy, Heidelberg and the Max Planck Institute for Extraterrestrial Physics, Garching, The Johns Hopkins University, Durham University, the University of Edinburgh, the Queen's University Belfast, the Harvard-Smithsonian Center for Astrophysics, the Las Cumbres Observatory Global Telescope Network Incorporated, the National Central University of Taiwan, the Space Telescope Science Institute, the National Aeronautics and Space Administration under Grant No. NNX08AR22G issued through the Planetary Science Division of the NASA Science Mission Directorate, the National Science Foundation Grant No. AST-1238877, the University of Maryland, Eotvos Lorand University (ELTE), the Los Alamos National Laboratory, and the Gordon and Betty Moore Foundation. Some of the data presented in this paper were obtained from the Mikulski Archive for Space Telescopes (MAST). STScI is operated by the Association of Universities for Research in Astronomy, Inc., under NASA contract NAS5-26555. This work is based in part on archival data obtained with the *Spitzer* Space Telescope, which is operated by the Jet Propulsion Laboratory, California Institute of Technology under a contract with NASA. This research has made use of NED which is operated by the Jet Propulsion Laboratory, California Institute of Technology, under contract with the National Aeronautics and Space Administration. We have made use of the Weizmann Interactive Supernova Data Repository (Yaron & Gal-Yam 2012, https://wiserep.weizmann.ac.il).

References

Alard, C. 2000, A&AS, 144, 363
Alard, C., & Lupton, R. H. 1998, ApJ, 503, 325
Aldering, G., Humphreys, R. M., & Richmond, M. 1994, AJ, 107, 662
Alonso-Herrero, A., Rieke, G. H., Rieke, M. J., et al. 2000, ApJ, 532, 845
Alonso-Herrero, A., Rieke, G. H., Rieke, M. J., et al. 2006, ApJ, 650, 835
Anderson, J. P., & Soto, M. 2013, A&A, 550, A69
Anderson, J. P., Habergham, S. M., & James, P. A. 2011, MNRAS, 416, 567
Anderson, J. P., Habergham, S. M., James, P. A., et al. 2012, MNRAS, 424, 1372
Anderson, J. P., González-Gaitán, S., Hamuy, M., et al. 2014, ApJ, 786, 67
Aramyan, L. S., Hakobyan, A. A., Petrosian, A. R., et al. 2016, MNRAS, 459, 3130
Arcavi, I., Gal-Yam, A., Yaron, O., et al. 2011, ApJ, 742, L18
Audcent-Ross, F. M., Meurer, G. R., Audcent, J. R., et al. 2020, MNRAS, 492, 848
Barnsley, R. M., Jermak, H. E., Steele, I. A., et al. 2016, J. Astron. Telesc. Instrum. Syst., 2, 015002
Bellm, E. C., Kulkarni, S. R., Graham, M. J., et al. 2019, PASP, 131, 018002
Bersten, M. C., Folatelli, G., García, F., et al. 2018, Nature, 554, 497
Berton, M., Bufano, F., Vogl, C., et al. 2018, ATel, 11160, 1
Bianco, F. B., Modjaz, M., Hicken, M., et al. 2014, ApJS, 213, 19
Bose, S., Holmbo, S., Mattila, S., et al. 2019, Transient Name Server Classification Report, 2019-1332, 1
Botticella, M. T., Pastorello, A., Smartt, S. J., et al. 2009, MNRAS, 398, 1041
Bruzual, G., & Charlot, S. 1993, ApJ, 405, 538
Bruzual, G., & Charlot, S. 2003, MNRAS, 344, 1000
Buckley, D. A. H., Swart, G. P., & Meiring, J. G. 2006, Proc. SPIE, 6267, 62670Z
Burgh, E. B., Nordsieck, K. H., Kobulnicky, H. A., et al. 2003, Proc. SPIE, 4841, 1463
Buzzoni, B., Delabre, B., Dekker, H., et al. 1984, The Messenger, 38, 9
Cardelli, J. A., Clayton, G. C., & Mathis, J. S. 1989, ApJ, 345, 245
Chambers, K. C., Magnier, E. A., Metcalfe, N., et al. 2016, ArXiv e-prints [arXiv:1612.05560]
Chu, J. K., Sanders, D. B., Larson, K. L., et al. 2017, ApJS, 229, 25
Crockett, R. M., Eldridge, J. J., Smartt, S. J., et al. 2008, MNRAS, 391, L5
Crowther, P. A. 2013, MNRAS, 428, 1927
Dahiwale, A., & Fremling, C. 2020, Transient Name Server Classification Report, 2020-927, 1
De, K. 2020, Transient Name Server Discovery Report, 2020-542, 1
Efstathiou, A., & Rowan-Robinson, M. 1995, MNRAS, 273, 649
Efstathiou, A., & Rowan-Robinson, M. 2003, MNRAS, 343, 322
Efstathiou, A., & Siebenmorgen, R. 2009, A&A, 502, 541
Efstathiou, A., Rowan-Robinson, M., & Siebenmorgen, R. 2000, MNRAS, 313, 734
Efstathiou, A., Christopher, N., Verma, A., et al. 2013, MNRAS, 436, 1873
Efstathiou, A., Małek, K., Burgarella, D., et al. 2021, MNRAS, 503, L11
Ekström, S., Georgy, C., Eggenberger, P., et al. 2012, A&A, 537, A146
Emonts, B. H. C., Piqueras-López, J., Colina, L., et al. 2014, A&A, 572, A40
Ergon, M., Sollerman, J., Fraser, M., et al. 2014, A&A, 562, A17
Ergon, M., Jerkstrand, A., Sollerman, J., et al. 2015, A&A, 580, A142
Fassia, A., Meikle, W. P. S., Vacca, W. D., et al. 2000, MNRAS, 318, 1093

Fenech, D. M., Muxlow, T. W. B., Beswick, R. J., et al. 2008, MNRAS, 391, 1384
Flaugher, B., Diehl, H. T., Honscheid, K., et al. 2015, AJ, 150, 150
Folatelli, G., Hamuy, M., Morrell, N., et al. 2004, IAU Circ., 8447
Folatelli, G., Bersten, M. C., Kuncarayakti, H., et al. 2014, ApJ, 792, 7
Folatelli, G., Bersten, M. C., Kuncarayakti, H., et al. 2015, ApJ, 811, 147
Galbany, L., Anderson, J. P., Sánchez, S. F., et al. 2018, ApJ, 855, 107
Gehrz, R. D., Sramek, R. A., & Weedman, D. W. 1983, ApJ, 267, 551
Heger, A., Fryer, C. L., Woosley, S. E., et al. 2003, ApJ, 591, 288
Herrero-Illana, R., Pérez-Torres, M. Á., Randriamanakoto, Z., et al. 2017, MNRAS, 471, 1634
Hodgkin, S. T., Breedt, E., Delgado, A., et al. 2019, Transient Name Server Discovery Report, 2019-1300, 1
Houck, J. R., Roellig, T. L., van Cleve, J., et al. 2004, ApJS, 154, 18
Hunter, D. J., Valenti, S., Kotak, R., et al. 2009, A&A, 508, 371
Huo, Z. Y., Xia, X. Y., Xue, S. J., et al. 2004, ApJ, 611, 208
Jencson, J. E., Kasliwal, M. M., Johansson, J., et al. 2017, ApJ, 837, 167
Jencson, J. E., Kasliwal, M. M., Adams, S. M., et al. 2018, ApJ, 863, 20
Jencson, J. E., Kasliwal, M. M., Adams, S. M., et al. 2019, ApJ, 886, 40
Jester, S., Schneider, D. P., Richards, G. T., et al. 2005, AJ, 130, 873
Johnson, S. P., Wilson, G. W., Tang, Y., & Scott, K. S. 2013, MNRAS, 436, 2535
Kangas, T., Portinari, L., Mattila, S., et al. 2017, A&A, 597, A92
Kankare, E., Mattila, S., Ryder, S., et al. 2008, ApJ, 689, L97
Kankare, E., Hanski, M., Theureau, G., & Teerikorpi, P. 2009, A&A, 493, 23
Kankare, E., Mattila, S., Ryder, S., et al. 2012, ApJ, 744, L19
Kankare, E., Fraser, M., Ryder, S., et al. 2014a, A&A, 572, A75
Kankare, E., Mattila, S., Ryder, S., et al. 2014b, MNRAS, 440, 1052
Kankare, E., Mattila, S., Ryder, S., et al. 2018a, ATel, 11156, 1
Kankare, E., Taubenberger, S., Vogl, C., et al. 2018b, ATel, 11778, 1
Kissler-Patig, M., Pirard, J.-F., Casali, M., et al. 2008, A&A, 491, 941
Kobulnicky, H. A., Nordsieck, K. H., Burgh, E. B., et al. 2003, Proc. SPIE, 4841, 1634
Kool, E. C. 2019, PhD Thesis, Macquarie University
Kool, E. C., Ryder, S., Kankare, E., et al. 2018, MNRAS, 473, 5641
Kotilainen, J. K., Moorwood, A. F. M., Ward, M. J., et al. 1996, A&A, 305, 107
Kuncarayakti, H., Maeda, K., Bersten, M. C., et al. 2015, A&A, 579, A95
Kuncarayakti, H., Anderson, J. P., Galbany, L., et al. 2018, A&A, 613, A35
Leloudas, G., Gallazzi, A., Sollerman, J., et al. 2011, A&A, 530, A95
Liu, Q.-Z., Hu, J.-Y., Hang, H.-R., et al. 2000, A&AS, 144, 219
Madau, P., & Dickinson, M. 2014, ARA&A, 52, 415
Magnelli, B., Elbaz, D., Chary, R. R., et al. 2011, A&A, 528, A35
Maiolino, R., Vanzi, L., Mannucci, F., et al. 2002, A&A, 389, 84
Masci, F. J., Laher, R. R., Rusholme, B., et al. 2019, PASP, 131, 995
Matheson, T., Filippenko, A. V., Ho, L. C., et al. 2000, AJ, 120, 1499
Mattila, S., & Meikle, W. P. S. 2001, MNRAS, 324, 325
Mattila, S., Väisänen, P., Farrah, D., et al. 2007, ApJ, 659, L9
Mattila, S., Dahlen, T., Efstathiou, A., et al. 2012, ApJ, 756, 111
Mattila, S., Fraser, M., Smartt, S. J., et al. 2013, MNRAS, 431, 2050
Mattila, S., Pérez-Torres, M., Efstathiou, A., et al. 2018, Science, 361, 482
Maund, J. R., Fraser, M., Ergon, M., et al. 2011, ApJ, 739, L37
Miluzio, M., Cappellaro, E., Botticella, M. T., et al. 2013, A&A, 554, A127
Modjaz, M., Blondin, S., Kirshner, R. P., et al. 2014, AJ, 147, 99
Moorwood, A., Cuby, J.-G., & Lidman, C. 1998, The Messenger, 91, 9
Morales-Garoffolo, A., Elias-Rosa, N., Benetti, S., et al. 2014, MNRAS, 445, 1647
Mould, J. R., Huchra, J. P., Freedman, W. L., et al. 2000, ApJ, 529, 786
Müller Bravo, T., Wiseman, P., Pursiainen, M., et al. 2019, Transient Name Server AstroNote, 155
Müller-Bravo, T. E., Gutiérrez, C. P., Sullivan, M., et al. 2020, MNRAS, 497, 361
Munari, U., Henden, A., Belligoli, R., et al. 2013, New Astron., 20, 30
Nayana, A. J., & Chandra, P. 2018, ATel, 11350, 1
Neff, S. G., Ulvestad, J. S., & Campion, S. D. 2003, ApJ, 599, 1043
Nomoto, K., Suzuki, T., Shigeyama, T., et al. 1993, Nature, 364, 507
Ohyama, Y., Terashima, Y., & Sakamoto, K. 2015, ApJ, 805, 162
Parra, R., Conway, J. E., Diamond, P. J., et al. 2007, ApJ, 659, 314
Pastorello, A., Zampieri, L., Turatto, M., et al. 2004, MNRAS, 347, 74
Pastorello, A., Valenti, S., Zampieri, L., et al. 2009, MNRAS, 394, 2266
Pastorello, A., Tartaglia, L., Elias-Rosa, N., et al. 2015, MNRAS, 454, 4293
Paufique, J., Bruton, A., Glindemann, A., et al. 2010, Proc. SPIE, 77361, 77361P
Pérez-Torres, M. A., Romero-Cañizales, C., Alberdi, A., et al. 2009, A&A, 507, L17
Pignata, G., Bauer, F. E., Forster, F., et al. 2020, Transient Name Server Discovery Report, 2020-909, 1
Podsiadlowski, P., Joss, P. C., & Hsu, J. J. L. 1992, ApJ, 391, 246
Podsiadlowski, P., Hsu, J. J. L., Joss, P. C., et al. 1993, Nature, 364, 509
Prentice, S. J., & Mazzali, P. A. 2017, MNRAS, 469, 2672
Pressberger, R., Maitzen, H. M., & Neely, A. W. 1993, IAU Circ, 5832, 2
Prieto, J. L., Kistler, M. D., Thompson, T. A., et al. 2008, ApJ, 681, L9
Randriamanakoto, Z., Väisänen, P., Ryder, S. D., et al. 2019, MNRAS, 482, 2530
Richmond, M. W., Treffers, R. R., Filippenko, A. V., et al. 1994, AJ, 107, 1022
Richmond, M. W., Treffers, R. R., Filippenko, A. V., et al. 1996, AJ, 112, 732
Ripero, J., Garcia, F., Rodriguez, D., et al. 1993, IAU Circ, 5731, 1
Romero-Cañizales, C., Mattila, S., Alberdi, A., et al. 2011, MNRAS, 415, 2688
Romero-Cañizales, C., Herrero-Illana, R., Pérez-Torres, M. A., et al. 2014, MNRAS, 440, 1067
Ryder, S., Kool, E., Kankare, E., et al. 2018, ATel, 11224, 1
Sahu, D. K., Anupama, G. C., Srividya, S., et al. 2006, MNRAS, 372, 1315
Sanders, D. B., Soifer, B. T., Elias, J. H., et al. 1988, ApJ, 325, 74
Sanders, D. B., Mazzarella, J. M., Kim, D.-C., Surace, J. A., & Soifer, B. T. 2003, AJ, 126, 1607
Schlafly, E. F., & Finkbeiner, D. P. 2011, ApJ, 737, 103
Silva, L., Granato, G. L., Bressan, A., & Danese, L. 1998, ApJ, 509, 103
Smartt, S. J. 2009, ARA&A, 47, 63
Smartt, S. J., Valenti, S., Fraser, M., et al. 2015, A&A, 579, A40
Smith, N., Ganeshalingam, M., Chornock, R., et al. 2009, ApJ, 697, L49
Smith, N., Li, W., Silverman, J. M., Ganeshalingam, M., & Filippenko, A. V. 2011, MNRAS, 415, 773
Soifer, B. T., Neugebauer, G., Matthews, K., et al. 2001, AJ, 122, 1213
Spiro, S., Pastorello, A., Pumo, M. L., et al. 2014, MNRAS, 439, 2873
Steele, I. A., Smith, R. J., Rees, P. C., et al. 2004, Proc. SPIE, 679
Stephens, M. A. 1974, J. Am. Stat. Assoc., 69, 347
Stritzinger, M., Taddia, F., Fransson, C., et al. 2012, ApJ, 756, 173
Stritzinger, M. D., Anderson, J. P., Contreras, C., et al. 2018a, A&A, 609, A134
Stritzinger, M. D., Taddia, F., Burns, C. R., et al. 2018b, A&A, 609, A135
Taddia, F., Sollerman, J., Leloudas, G., et al. 2015, A&A, 574, A60
Taddia, F., Stritzinger, M. D., Bersten, M., et al. 2018, A&A, 609, A136
Tomasella, L., Benetti, S., Ochner, P., et al. 2020, ATel, 13616, 1
Trancho, G., Bastian, N., Miller, B. W., et al. 2007, ApJ, 664, 284
Tully, R. B. 1988, Nearby Galaxies Catalog (Cambridge: Cambridge University Press), 221
Ulvestad, J. S. 2009, AJ, 138, 1529
Valenti, S., Fraser, M., Benetti, S., et al. 2011, MNRAS, 416, 3138
Van Dyk, S. D., Li, W., Cenko, S. B., et al. 2011, ApJ, 741, L28
Van Dyk, S. D., Zheng, W., Fox, O. D., et al. 2014, AJ, 147, 37
Varenius, E., Conway, J. E., Batejat, F., et al. 2019, A&A, 623, A173
Wong, O. I., Ryan-Weber, E. V., Garcia-Appadoo, D. A., et al. 2006, MNRAS, 371, 1855
Woosley, S. E. 2019, ApJ, 878, 49
Woosley, S. E., Eastman, R. G., Weaver, T. A., et al. 1994, ApJ, 429, 300
Yaron, O., & Gal-Yam, A. 2012, PASP, 124, 668
Yuan, F., Jerkstrand, A., Valenti, S., et al. 2016, MNRAS, 461, 2003

[1] Tuorla Observatory, Department of Physics and Astronomy, University of Turku, 20014 Turku, Finland
e-mail: erkki.kankare@utu.fi
[2] School of Sciences, European University Cyprus, Diogenes Street, Engomi 1516 Nicosia, Cyprus
[3] The Oskar Klein Centre, Department of Astronomy, Stockholm University, AlbaNova 10691 Stockholm, Sweden
[4] Space Telescope Science Institute, 3700 San Martin Drive, Baltimore, MD 21218, USA
[5] Astrophysics Research Centre, School of Mathematics and Physics, Queen's University Belfast, Belfast BT7 1NN, UK
[6] South African Astronomical Observatory, PO Box 9, Observatory 7935, Cape Town, South Africa
[7] Southern African Large Telescope, PO Box 9, Observatory 7935, Cape Town, South Africa
[8] Department of Astronomy, University of Cape Town, Private Bag X3, Rondebosch 7701, South Africa
[9] Department of Physics and Astronomy, Macquarie University, NSW 2109, Australia
[10] Macquarie University Research Centre for Astronomy, Astrophysics & Astrophotonics, Sydney, NSW 2109, Australia
[11] Parkdale Observatory, 225 Warren Road, RDl Oxford, Canterbury 7495, New Zealand
[12] Backyard Observatory Supernova Search (BOSS), New Zealand

[13] School of Physics, O'Brien Centre for Science North, University College Dublin, Belfield, Dublin 4, Ireland
[14] INAF – Osservatorio Astronomico, Vicolo Osservatorio 5, 35122 Padova, Italy
[15] Astrophysics Research Institute, Liverpool John Moores University, IC2, Liverpool Science Park, 146 Brownlow Hill, Liverpool L3 5RF, UK
[16] Max-Planck-Institut für Astrophysik, Karl-Schwarzschild-Str. 1, 85748 Garching, Germany
[17] Dipartimento di Fisica e Astronomia, Universitá di Padova, Vicolo Osservatorio 2, 35122 Padova, Italy
[18] Finnish Centre for Astronomy with ESO (FINCA), University of Turku, Vesilinnantie 5, 20014 Turku, Finland
[19] Instituto de Astrofísica de Andalucía, Glorieta de las Astronomía, s/n, 18008 Granada, Spain
[20] Departamento de Física Teorica, Facultad de Ciencias, Universidad de Zaragoza, Zaragoza, Spain
[21] Institute of Astronomy and Astrophysics, Academia Sinica, 11F of Astronomy-Mathematics Building, AS/NTU No. 1, Sec. 4, Roosevelt Rd, Taipei 10617, Taiwan ROC
[22] Aalto University Metsähovi Radio Observatory, Metsähovintie 114, 02540 Kylmälä, Finland
[23] Cerro Tololo Inter-American Observatory, NSF's National Optical-Infrared Astronomy Research Laboratory, Casilla 603, La Serena, Chile
[24] Departamento de Física Teórica y del Cosmos, Universidad de Granada, 18071 Granada, Spain
[25] Astronomical Observatory, University of Warsaw, Al. Ujazdowskie 4, 00-478 Warszawa, Poland
[26] School of Physics & Astronomy, Cardiff University, Queens Buildings, The Parade, Cardiff CF24 3AA, UK
[27] School of Physics, Trinity College Dublin, The University of Dublin, Dublin 2, Ireland
[28] School of Physics and Astronomy, University of Southampton, Southampton, Hampshire SO17 1BJ, UK
[29] Birmingham Institute for Gravitational Wave Astronomy and School of Physics and Astronomy, University of Birmingham, Birmingham B15 2TT, UK
[30] Institute for Astronomy, University of Edinburgh, Royal Observatory, Blackford Hill EH9 3HJ, UK
[31] Departamento de Ciencias Físicas, Universidad Andrés Bello, Avda. República 252, Santiago, Chile
[32] Millennium Institute of Astrophysics, Nuncio Monsenor Sótero Sanz 100, Providencia, Santiago, Chile

Appendix A: SN 2020cuj in NGC 1614

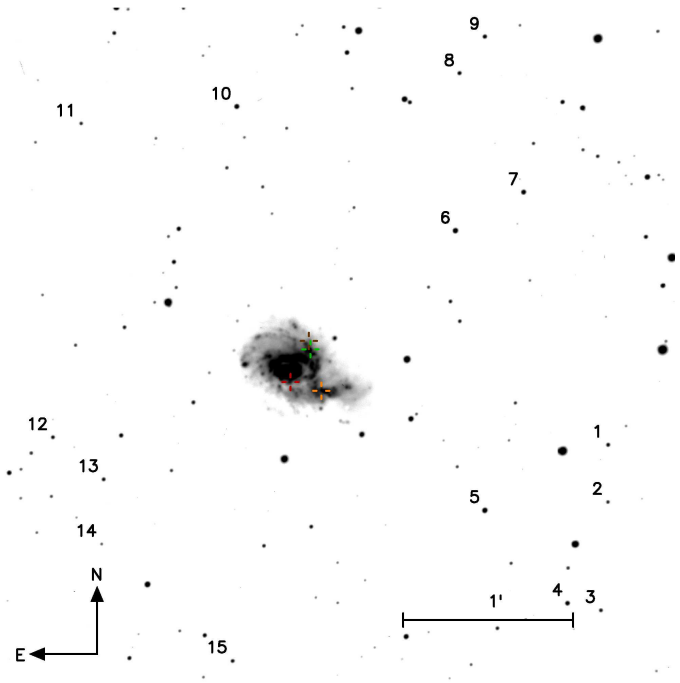

Fig. A.1. 4′ × 4′ ePESSTO NTT+EFOSC2 *r*-band image of the field of NGC 3256 on 2018 January 16. The locations of the sequence stars (numbered) and the SNe are indicated: SN 2018ec (green), AT 2018cux (red), PSN102750 (brown), and SN 2001db (orange). North is up, east is left.

SN 2020cuj in NGC 1614 was discovered by ZTF on 2020 February 12 03:06:02 UT with the internal name of ZTF20aaoffej (De 2020), and classified by Dahiwale & Fremling (2020) as a Type II SN. The SN was also detected by *Gaia* (internal name Gaia20ayu). *Gaia* derives coordinates RA = $04^{h}34^{m}00\overset{s}{.}53$ and Dec = $-08°34'43\overset{''}{.}46$ for the SN. We took the public photometry of SN 2020cuj obtained by these surveys, and also measured the template image subtracted magnitudes from a NTT+EFOSC2 (via ePESSTO+) image of $m_V = 19.28 \pm 0.06$ mag (on JD = 2458905.53), and a NOT+NOTCam image of $m_K = 15.74 \pm 0.04$ mag (on JD = 2458912.37). Based on a light curve fit with the Type IIP SN 2013ej (Yuan et al. 2016) as a template we find that SN 2020cuj was discovered shortly after the explosion, has a host galaxy extinction of $A_V = 2.8 \pm 0.2$ mag, and is $0.6^{+0.1}_{-0.2}$ mag brighter than SN 2013ej. The light curve fit is shown in Fig. A.2. The late-time *Gaia* detection could indicate a more linearly declining Type IIL SN; however, the *Gaia* data points are not template subtracted and likely contain background contamination from the host galaxy, which can be significant at late phases.

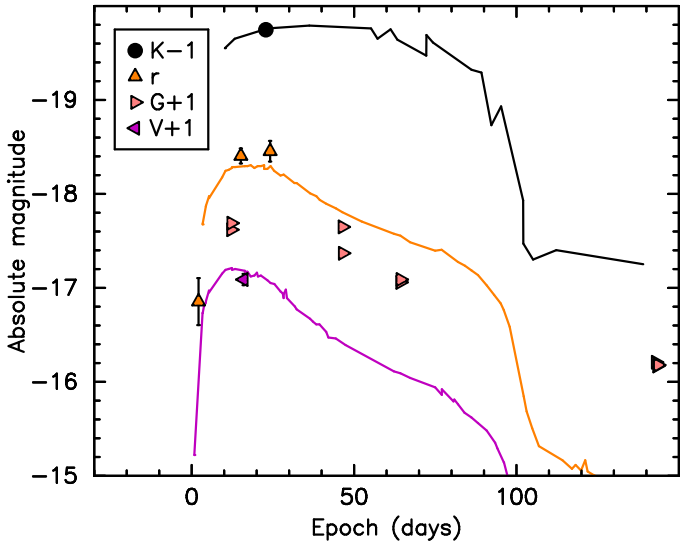

Fig. A.2. Absolute magnitude light curves of AT 2020cuj (points) in NGC 1614 corrected for the host galaxy extinction of $A_V = 2.8$ mag, estimated with a fit to the light curves of the Type IIP SN 2013ej (solid lines, Yuan et al. 2016). The epoch 0 is set to the estimated explosion date of SN 2013ej. Since the *Gaia* light curve is not template subtracted, it is likely that it contains flux excess from the luminous host background, which has an effect, particularly on the late-time data points.

We note that public ZTF brokers also list another event: ZTF19acyfumm in NGC 1614 at RA = $04^{h}34^{m}00\overset{s}{.}06$ and Dec = $-08°34'44\overset{''}{.}47$ discovered on 2019 November 25 07:59:00 UT. The coordinates are consistent with the host galaxy nucleus, but not with SN 2020cuj, and the two events appear to be unrelated. The ePESSTO+ programme obtained an optical spectrum at the location on 2019 December 18 with the NTT and EFOSC2; however, the spectrum was reported to be red and dominated by the host galaxy without clear transient features (Müller Bravo et al. 2019). To our knowledge no other transient programme has carried out any observations of ZTF19acyfumm, and due to the unclear nature of the event it is not part of our study.

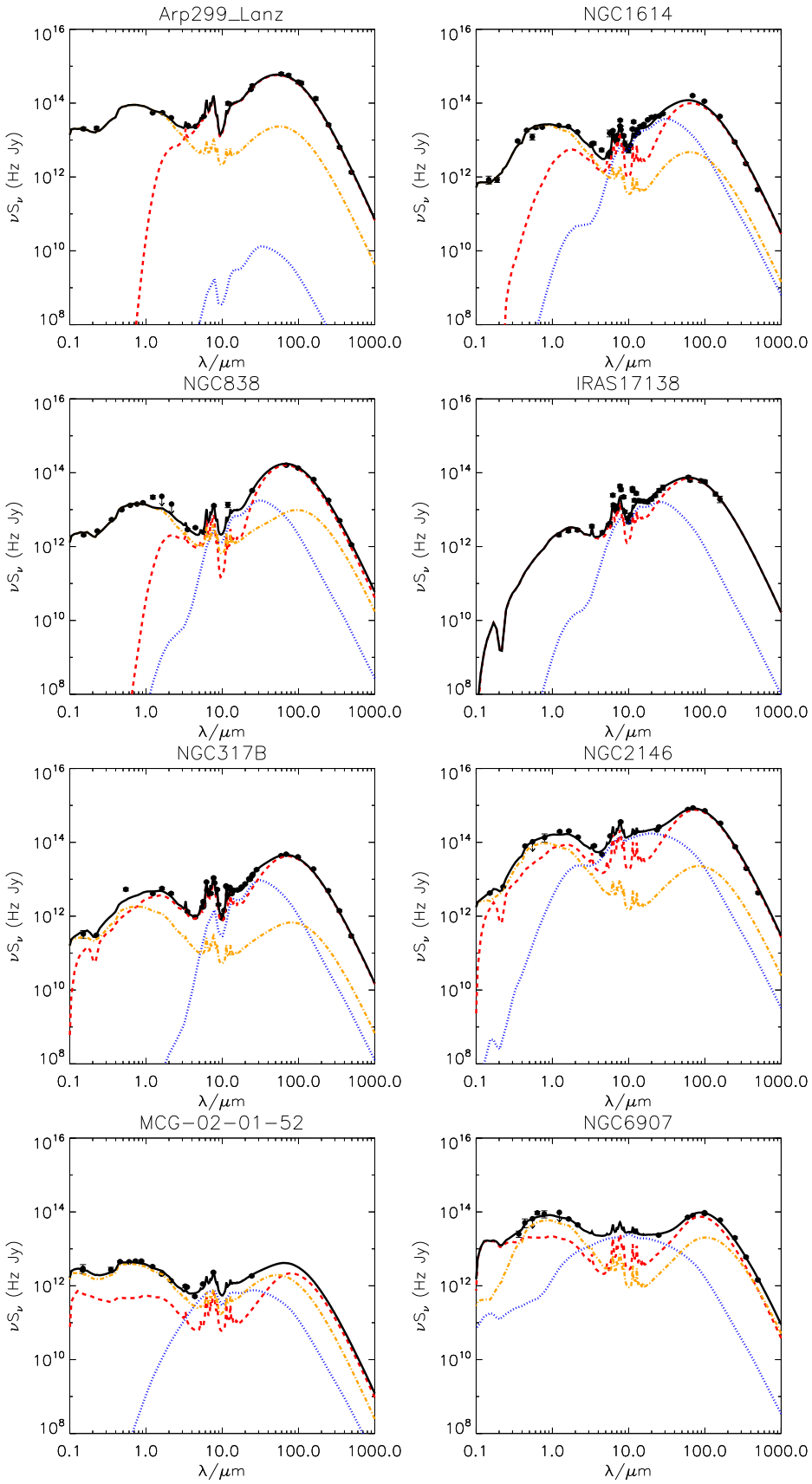

Fig. A.3. Our SED models (solid black curves) for the observations (black points) of our initial sample of LIRGs for which a spherical host galaxy model is favoured. The model components include a spheroidal galaxy (dot-dashed orange), starburst contribution (dashed red), and an AGN (dotted blue).

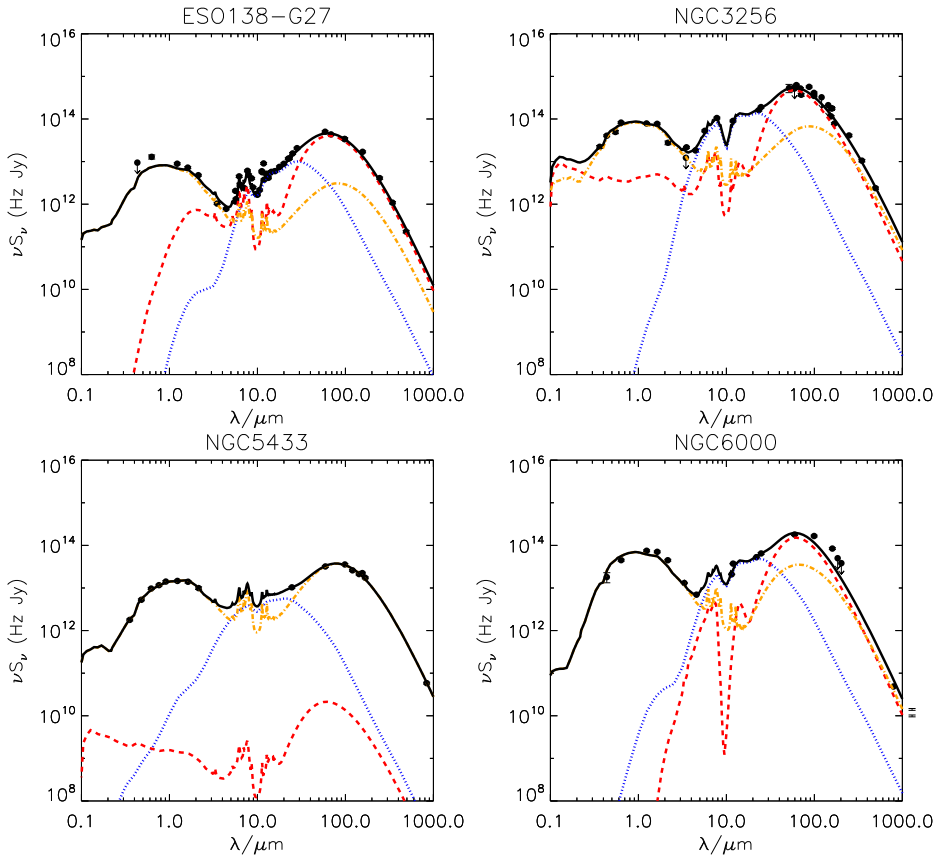

Fig. A.3. continued.

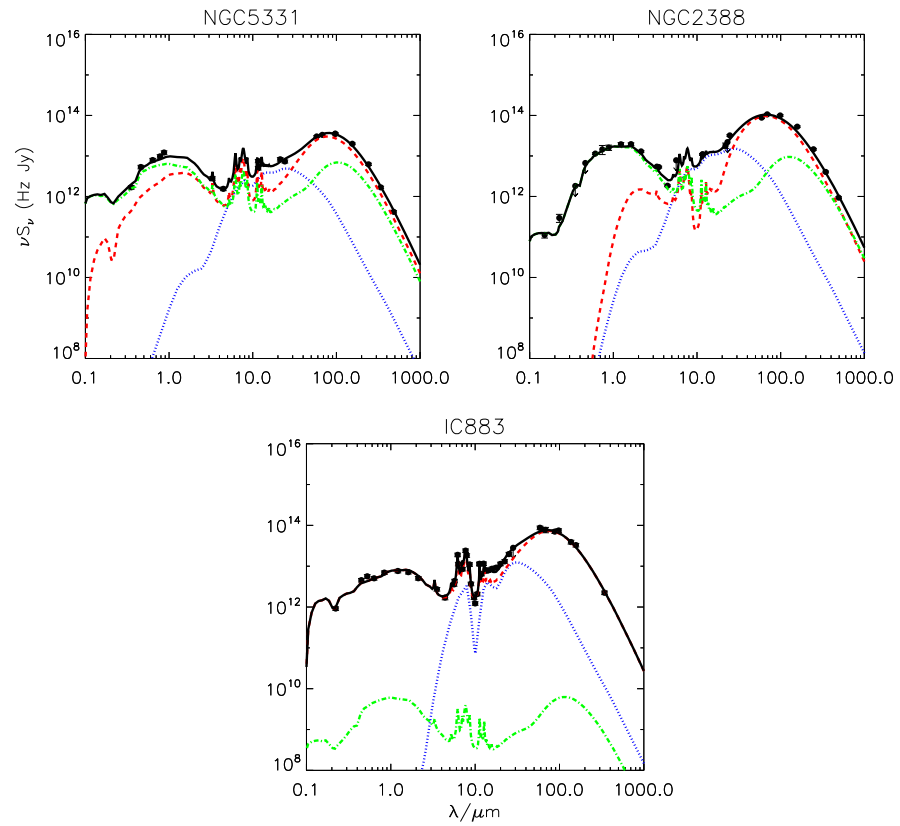

Fig. A.4. Our SED models (solid black curves) for the observations (black points) of our initial sample of LIRGs for which a disc host galaxy model is favoured. The model components include a disc galaxy (dot-dashed green), starburst contribution (dashed red), and an AGN (dotted blue).

Table A.1. Optical sequence star magnitudes in the field of SN 2018ec.

No.	m_g (mag)	m_r (mag)	m_i (mag)	m_z (mag)
1	18.538(0.014)	17.920(0.018)	17.703(0.019)	17.603(0.042)
2	19.121(0.015)	18.364(0.018)	18.101(0.019)	17.973(0.048)
3	18.741(0.014)	18.115(0.017)	17.862(0.019)	17.786(0.059)
4	17.824(0.012)	17.400(0.018)	17.221(0.018)	17.121(0.050)
5	17.557(0.014)	16.782(0.017)	16.482(0.018)	16.232(0.023)
6	17.176(0.014)	16.726(0.018)	16.545(0.019)	16.366(0.019)
7	18.022(0.015)	17.170(0.018)	16.840(0.019)	16.594(0.022)
8	18.532(0.016)	17.797(0.017)	17.537(0.020)	17.318(0.020)
9	18.180(0.014)	17.644(0.017)	17.429(0.019)	17.253(0.022)
10	17.547(0.014)	17.066(0.018)	16.881(0.019)	16.667(0.021)
11	18.892(0.016)	18.376(0.018)	18.163(0.020)	18.026(0.030)
12	18.509(0.016)	18.026(0.018)	17.820(0.020)	17.605(0.018)
13	19.572(0.021)	18.125(0.018)	16.861(0.020)	16.284(0.018)
14	19.602(0.019)	18.873(0.043)	18.729(0.020)	18.437(0.018)
15	18.521(0.014)	18.114(0.018)	17.943(0.020)	17.671(0.022)

Notes. The errors are given in brackets.

Table A.2. Photometry for SN 2018ec.

JD (2400000+)	m_g (mag)	m_r (mag)	m_i (mag)	m_z (mag)	m_J (mag)	m_H (mag)	m_K (mag)	Telescope
58121.86	–	–	–	–	–	–	15.13(0.05)	VLT
58124.86	–	–	–	–	–	–	15.22(0.04)	VLT
58130.76	–	–	–	17.15(0.03)	–	–	–	NTT
58134.77	–	–	–	–	16.35(0.04)	15.79(0.03)	15.72(0.05)	NTT
58135.71	20.25(0.03)	18.79(0.06)	18.02(0.01)	17.40(0.03)	–	–	–	NTT
58154.82	–	–	–	–	17.04(0.09)	16.30(0.03)	16.37(0.06)	NTT
58162.83	20.74(0.07)	19.16(0.07)	18.48(0.02)	17.85(0.03)	–	–	–	NTT
58164.86	–	–	–	–	17.38(0.10)	16.51(0.04)	16.62(0.06)	NTT
58169.80	20.89(0.06)	19.31(0.10)	18.70(0.03)	18.04(0.03)	–	–	–	NTT
58186.61	–	–	–	–	–	–	17.08(0.16)	NTT
58186.79	20.97(0.17)	19.64(0.15)	19.02(0.03)	18.32(0.08)	–	–	–	NTT
58201.70	21.21(0.07)	19.67(0.12)	19.20(0.03)	18.62(0.04)	–	–	–	NTT
58204.61	–	–	–	–	18.64(0.20)	17.51(0.06)	17.44(0.10)	NTT
58215.72	21.38(0.23)	20.01(0.17)	19.41(0.05)	18.98(0.07)	–	–	–	NTT
58216.53	–	–	–	–	18.71(0.41)	17.52(0.10)	17.76(0.11)	NTT
58228.57	–	20.29(0.20)	19.72(0.05)	19.12(0.09)	–	–	–	NTT
58230.58	–	–	–	–	18.84(0.29)	–	–	NTT
58243.55	–	20.11(0.20)	19.94(0.04)	19.37(0.06)	–	–	–	NTT
58250.65	–	20.72(0.45)	20.09(0.04)	19.67(0.06)	–	–	–	NTT
58251.58	–	–	–	–	19.04(0.25)	18.47(0.15)	18.42(0.30)	NTT
58260.46	–	20.15(0.27)	20.17(0.05)	19.85(0.08)	–	–	–	NTT

Notes. The errors are given in brackets.

Table A.3. Spectroscopic log for SN 2018ec.

JD (2400000+)	Epoch (d)	Grism	Slit ($''$)	R ($\lambda/\Delta\lambda$)	PA ($^\circ$)	Exp. time (s)	λ (Å)	Telescope
58130.8	+28	Gr13	1.0	355	121	1500	3645–9235	NTT
58134.7	+32	GB	1.0	550	0	$12\times3\times90$	9370–16 460	NTT
58135.7	+33	Gr13	1.0	355	83,91	2×2700	3640–9230	NTT
58154.7	+52	GB	1.0	550	0	$6\times3\times90$	9370–16 460	NTT
58164.8	+62	GB	1.0	550	0	$12\times3\times90$	9370–16 460	NTT
58165.8	+63	Gr13	1.0	355	228,249	2×2700	3645–9235	NTT
58187.8	+85	Gr13	1.0	355	236,252	2×2400	3645–9235	NTT

Table A.4. Photometry for AT 2018cux.

JD (2400000+)	m_g (mag)	m_r (mag)	m_i (mag)	m_z (mag)	m_J (mag)	m_H (mag)	m_K (mag)	Telescope
58169.81	>22.9	>22.3	>21.5	>20.2	–	–	–	NTT
58186.80	>21.7	>21.8	>20.5	>19.7	–	–	–	NTT
58187.74	–	–	–	>20.9	–	–	–	NTT
58201.70	22.05(0.44)	20.91(0.20)	20.56(0.14)	20.12(0.13)	–	–	–	NTT
58204.62	–	–	–	–	18.67(0.24)	18.36(0.51)	18.08(0.62)	NTT
58215.72	22.19(0.25)	20.83(0.29)	20.26(0.21)	19.82(0.35)	–	–	–	NTT
58216.52	–	–	–	–	18.79(0.24)	17.80(0.36)	>17.9	NTT
58228.58	–	20.53(0.12)	20.01(0.07)	19.94(0.08)	–	–	–	NTT
58230.57	–	–	–	–	18.73(0.17)	–	–	NTT
58243.54	–	20.58(0.03)	20.01(0.13)	19.63(0.09)	–	–	–	NTT
58250.65	–	20.58(0.06)	19.91(0.07)	19.79(0.09)	–	–	–	NTT
58251.55	–	–	–	–	18.34(0.17)	18.01(0.31)	17.56(0.55)	NTT
58260.46	–	20.46(0.02)	19.92(0.06)	19.55(0.06)	–	–	–	NTT

Notes. The errors are given in brackets.

Table A.5. Photometry for PSN102750.

JD (2400000+)	m_B (mag)	m_R (mag)	Telescope
56785.93	–	15.67(0.22)	T30
56793.41	–	15.37(0.15)	C14
56813.38	–	15.95(0.13)	C14
56818.84	17.065(0.001)	–	HST
56975.16	–	19.116(0.004)	HST

Notes. The errors are given in brackets.

Table A.6. Our photometry for SN 2019lqo.

JD (2400000+)	m_U (mag)	m_B (mag)	m_V (mag)	m_R (mag)	m_I (mag)	m_J (mag)	m_H (mag)	m_K (mag)	Telescope
58689.37	–	–	–	17.77(0.08)	–	–	–	–	NOT
58694.39	19.13(0.12)	19.03(0.07)	17.92(0.03)	17.42(0.02)	17.01(0.02)	–	–	–	NOT
58699.38	19.21(0.07)	18.93(0.08)	17.77(0.02)	17.22(0.02)	16.75(0.02)	–	–	–	NOT
58706.36	19.96(0.25)	19.48(0.12)	17.88(0.03)	17.24(0.03)	16.77(0.03)	–	–	–	NOT
58712.37	–	20.11(0.33)	18.10(0.04)	17.44(0.03)	16.90(0.03)	–	–	–	NOT
58714.36	–	–	–	–	–	16.18(0.02)	15.95(0.04)	–	NOT
58780.70	–	–	–	–	–	17.95(0.04)	17.19(0.04)	16.97(0.09)	NOT
58864.56	–	–	21.31(0.18)	20.49(0.06)	19.97(0.06)	–	–	–	NOT

Notes. The errors are given in brackets.

Table A.7. Photometry for SN 2019lqo based on public data including our measurements from the ZTF DR3.

JD (2400000+)	m_g (mag)	m_G (mag)	m_r (mag)	Telescope
58679.68	20.27(0.15)	–	–	ZTF
58679.70	–	–	19.04(0.09)	ZTF
58680.73	–	>21.5	–	*Gaia*
58683.71	–	–	18.77(0.12)	ZTF
58685.82	–	18.33(0.20)	–	*Gaia*
58686.68	19.13(0.09)	–	–	ZTF
58766.01	20.13(0.15)	–	–	ZTF
58770.99	–	–	18.87(0.11)	ZTF
58777.01	–	–	19.05(0.12)	ZTF
58786.01	–	–	19.15(0.06)	ZTF
58791.01	–	–	19.20(0.11)	ZTF
58793.01	–	–	19.42(0.09)	ZTF
58794.02	–	–	19.42(0.07)	ZTF
58805.04	–	–	19.65(0.14)	ZTF
58807.05	–	–	19.53(0.10)	ZTF
58813.06	–	–	19.60(0.14)	ZTF
58828.92	–	–	19.87(0.20)	ZTF
58830.95	–	–	20.01(0.16)	ZTF
58833.93	–	–	19.91(0.23)	ZTF
58836.98	–	–	19.82(0.11)	ZTF
58846.97	–	–	20.36(0.30)	ZTF

Notes. The errors are given in brackets.

Table A.8. Our optical photometry for SN 2020fkb.

JD (2400000+)	m_u (mag)	m_B (mag)	m_g (mag)	m_V (mag)	m_r (mag)	m_i (mag)	m_z (mag)	Telescope
58936.66	–	–	17.83(0.08)	–	–	–	–	ZTF
58939.62	–	–	–	–	16.97(0.07)	–	–	ZTF
58939.83	–	–	17.33(0.07)	–	–	–	–	ZTF
58939.87	–	–	–	–	16.93(0.09)	–	–	ZTF
58942.33	–	17.53(0.11)	17.17(0.04)	17.00(0.07)	16.85(0.09)	17.04(0.05)	17.00(0.11)	A1.82 m
58943.30	–	17.38(0.04)	–	16.80(0.06)	16.72(0.05)	16.86(0.03)	16.99(0.07)	A1.82 m
58944.44	17.98(0.11)	17.51(0.24)	16.88(0.04)	16.75(0.06)	16.56(0.04)	16.75(0.03)	16.79(0.07)	A1.82 m
58945.31	18.61(0.57)	17.44(0.11)	16.88(0.04)	16.87(0.06)	16.63(0.03)	16.78(0.04)	16.85(0.04)	A1.82 m
58947.32	18.26(0.41)	17.41(0.09)	16.94(0.09)	16.69(0.04)	16.45(0.08)	16.36(0.09)	–	A67/92 cm
58948.32	18.55(0.41)	17.46(0.04)	17.05(0.06)	16.62(0.07)	16.50(0.11)	16.43(0.13)	–	A67/92 cm
58949.33	18.54(0.49)	17.48(0.07)	17.02(0.08)	16.74(0.06)	16.37(0.09)	16.36(0.18)	–	A67/92 cm
58949.40	18.34(0.36)	17.40(0.04)	17.00(0.02)	16.60(0.01)	16.48(0.04)	16.49(0.01)	16.52(0.02)	LT
58950.37	–	17.63(0.06)	17.10(0.10)	16.74(0.08)	16.41(0.08)	16.47(0.13)	–	A67/92 cm
58955.44	–	18.31(0.08)	17.70(0.05)	17.10(0.04)	16.77(0.07)	16.65(0.03)	16.73(0.05)	A1.82 m
58960.52	–	19.01(0.09)	17.99(0.05)	17.37(0.02)	17.03(0.03)	16.75(0.01)	16.72(0.03)	NOT
58962.42	–	19.13(0.23)	18.30(0.31)	17.66(0.12)	17.29(0.37)	16.86(0.17)	–	A67/92 cm
58969.42	–	19.42(0.08)	18.58(0.07)	17.93(0.03)	17.63(0.06)	17.23(0.02)	17.02(0.04)	NOT
58976.42	–	19.57(0.05)	18.82(0.08)	18.13(0.02)	18.01(0.07)	17.56(0.04)	17.17(0.05)	NOT
58989.45	–	20.37(0.16)	18.95(0.12)	18.57(0.04)	18.24(0.07)	17.82(0.03)	17.33(0.07)	NOT
58999.38	–	20.03(0.10)	19.05(0.12)	18.74(0.25)	18.48(0.08)	18.06(0.03)	17.38(0.06)	NOT
59011.40	–	–	19.03(0.14)	18.86(0.18)	18.64(0.14)	18.27(0.09)	17.59(0.08)	NOT
59021.42	–	20.59(0.21)	19.32(0.19)	18.94(0.04)	18.76(0.07)	18.45(0.05)	17.73(0.08)	NOT
59033.43	–	–	19.55(0.20)	19.16(0.07)	19.17(0.21)	18.79(0.07)	17.92(0.11)	NOT
59049.38	–	–	19.53(0.21)	19.38(0.11)	19.38(0.19)	19.15(0.16)	18.18(0.10)	NOT

Notes. The errors are given in brackets, and the early public ZTF photometry is listed for completeness.

Table A.9. Our near-IR photometry for SN 2020fkb.

JD (2400000+)	m_J (mag)	m_H (mag)	m_K (mag)	Telescope
58945.37	–	15.95(0.05)	–	LT
58964.45	–	15.69(0.08)	–	LT
58970.38	–	15.88(0.04)	–	LT
58974.36	–	15.99(0.04)	–	LT
58978.44	16.43(0.04)	–	15.88(0.13)	NOT
58979.45	–	16.31(0.05)	–	LT
59000.39	17.09(0.06)	16.68(0.08)	16.60(0.06)	NOT
59025.47	17.95(0.16)	17.55(0.14)	17.34(0.35)	NOT

Notes. The errors are given in brackets.

Table A.10. Spectroscopic log for SN 2020fkb.

JD (2400000+)	Epoch (d)	Grism	Slit ($''$)	R ($\lambda/\Delta\lambda$)	PA ($^\circ$)	Exp. time (s)	λ (Å)	Telescope
58942.3	−7	Gr4	1.7	310	259	2700	3400−8200	A1.82 m
58943.3	−6	Gr4	1.7	310	265	1800	3400−8200	A1.82 m
58945.4	−4	Gr4	1.7	310	203	1800	3400−8200	A1.82 m
58956.4	+7	Gr4	1.7	310	126	3600	3400−8175	A1.82 m
58968.5	+20	Gr4	1.3	280	124	1800	3500−9300	NOT
59021.4	+72	Gr4	1.3	280	122	2400	3400−9300	NOT
59036.4	+87	Gr4	1.3	280	101	2400	3500−9300	NOT